Nano Today (2013) 8, 619—642

Available online at www.sciencedirect.com

ScienceDirect

journal homepage: www.elsevier.com/locate/nanotoday

REVIEW

# Piezotronics and piezo-phototronics — From single nanodevices to array of devices and then to integrated functional system

Wenzhuo Wu[a], Caofeng Pan[a,b], Yan Zhang[a,b], Xiaonan Wen[a], Zhong Lin Wang[a,b,*]

[a] School of Materials Science and Engineering, Georgia Institute of Technology, Atlanta, GA 30332-0245, United States
[b] Beijing Institute of Nanoenergy and Nanosystems, Chinese Academy of Sciences, China

Received 4 October 2013; received in revised form 19 November 2013; accepted 28 November 2013
Available online 30 December 2013

**KEYWORDS**
Piezopotential;
Piezotronics;
Piezo-phototronics;
LED;
Sensors

**Summary** Due to the polarization of ions in a crystal that has non-central symmetry in piezoelectric-semiconductors such as ZnO, GaN and InN, piezoelectric polarization charges are created at the interface region by applying a strain, which created a potential (piezopotential) in the crystal. Piezotronics is about the devices fabricated using the piezopotential as a ''gate'' voltage to tune/control charge carrier transport at a contact or junction. The piezo-phototronic effect is to use the piezopotential to control the carrier generation, transport, separation and/or recombination for improving the performance of optoelectronic devices, such as solar cell and LED. Starting from the fundamental physics principles, this article gives an updated review about the fabrication of array of piezotronic devices so that they can be integrated into a system for achieving specific functions as sensors and MEMS. This first demonstration of fabricating array of piezotronic devices and integrated them into a system is a major milestone in nanotechnology, and it represents one of the promising directions of nanoelectronics.


## Introduction

Enabling technologies for developing electronics with tunable functionalities are critical to emerging applications in consumer electronics, prosthetic devices, robotics, surgical instruments and biomedical therapy/treatments [1—7], in which the active and adaptive interactions between electronic devices and stimuli from the ambient environment/host (e.g. human body) are essential. Mechanical stimuli are ubiquitous and abundant in the environment

* Corresponding author at: School of Materials Science and Engineering, Georgia Institute of Technology, Atlanta, GA 30332-0245, United States.
*E-mail addresses:* zlwang@gatech.edu, zhong.wang@mse.gatech.edu (Z.L. Wang).

1748-0132/$ — see front matter © 2013 Elsevier Ltd. All rights reserved.
http://dx.doi.org/10.1016/j.nantod.2013.11.002

for interacting with or controlling the electronics in micro/nano-systems [8—10]. It is, however, not facile to directly interface mechanical actuations using silicon electronics, nor is it straightforward to utilize these mechanical sources to control electronic devices. Producing polarization charges in response to mechanical deformation due to the linear coupling between mechanical and electrical states in materials which lack inversion symmetry, piezoelectric effect has been widely utilized for electromechanical sensing, actuating and mechanical energy harvesting [11]. Nevertheless, conventional piezoelectric materials such as perovskite-structured $Pb(Zr_xTi_{1-x})O_3$ (PZT) and polyvinylidene fluoride (PVDF) are electrically insulating and hence not feasible for constructing functional electronics. The influence of mechanically induced polarization charges on charge carriers in piezoelectric materials has consequently been long overlooked. Semiconductor materials such as ZnO, GaN and CdS with wurtzite or zinc blende structure also possess piezoelectric properties but are not as extensively utilized in piezoelectric sensors and actuators due to their relatively small piezoelectric coefficients [12]. The coupling of piezoelectric polarization with semiconductor properties in these materials has resulted in both novel fundamental phenomenon and unprecedented device applications, leading to the increasing research interests in the emerging field of *piezotronics* since its first introduction in 2006 [8,9,13,14]. The core of piezotronics lies in the fact that strain-induced polarization charges at interface can effectively modulate the local interfacial band structure and hence the charge carrier transport across junction/contact formed in piezoelectric semiconductor devices, by exerting substantial influence on the concentration/distribution of free carriers and interfacial electronic charged states in the device. The fundamental of piezotronics was reviewed previously [12]. This paper intends to provide a review on the fundamental physics involved, recent progress achieved and application prospects in the research of piezotronics. Our specific emphasis is on the paradigm shift of fabricating single devices to an array of devices for building integrated system. This is a milestone progress in the field of nanotechnology.

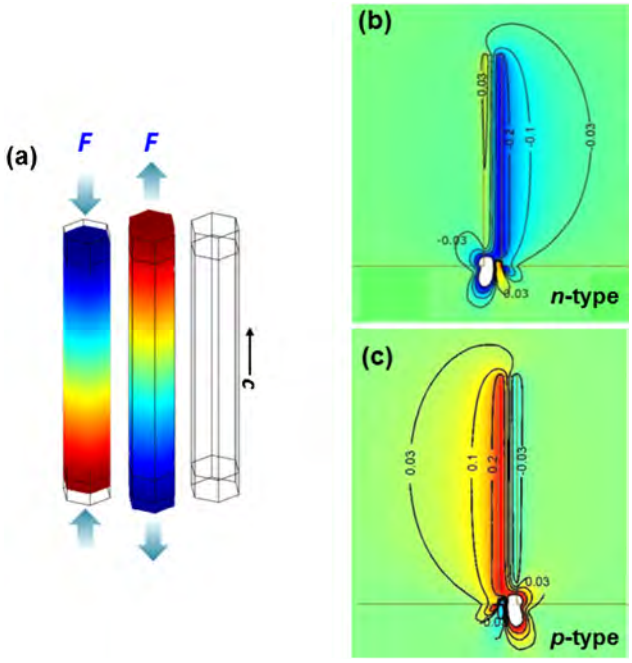


**Figure 1** Strain-induced polarization in piezoelectric semiconductor. (a) Left, distribution of piezopotential along a ZnO NW under axial strain calculated by numerical methods. (Reprinted with permission from [15]. Copyright 2009 AIP Publishing LLC.) (b) Numerical calculation results of the piezopotential distribution in an *n*-type ZnO NW considering finite doping with donor concentration of $1 \times 10^{17}\,cm^{-3}$. (Reprinted with permission from [17]. Copyright 2009 American Chemical Society.). (c) Numerical calculation results of the piezopotential distribution when the acceptor concentration in the ZnO NW is $1 \times 10^{17}\,cm^{-3}$. (Reprinted with permission from [20]. Copyright 2009 American Chemical Society.) The color gradient represents the distribution of piezopotential in which red indicates positive piezopotential and blue indicates negative piezopotential. The growth direction of the NW is along *c*-axis. (For interpretation of the references to color in this figure legend, the reader is referred to the web version of the article.)

## Fundamental physics of piezotronics

### Piezoelectric polarization in strained ZnO

Zinc oxide is used as the modular material system to elaborate the fundamental effect in piezotronics. It is chosen not only because it is a representative piezoelectric semiconductor material, but also for its easy, low-cost and controlled synthesis at low temperature. The same principle applies to other piezoelectric semiconductors, such as GaN, InN, CdS and more. The absence of inversion symmetry gives rise to non-mobile piezoelectric polarization charges at the interfaces in wurtzite-structured ZnO crystal upon mechanical straining. The effect of piezoelectric polarization can be partially screened by the moderate-level doping, but cannot be completely diminished due to the dielectric property of the material. These interfacial ionic charges are capable of inducing considerable modulation to charge carrier distribution in ZnO and the adjacent semiconductor/metal which forms junction/contact with ZnO [8].

Theoretical investigation has been performed on the distribution of electric field (i.e. piezopotential) induced by the piezoelectric polarization in strained ZnO nanowire (NW). Axially strained NW with its two ends in contact with metal electrodes on the flexible substrate constitutes the most common configuration for ZnO NW based piezotronic device. The dimension of NWs is orders of magnitude smaller than that of the substrates so that the mechanical behavior of the entire device is dictated by the substrate. By ignoring the body force and free charge carriers in the NW for simplicity, the piezopotential is found to distribute continuously in the NW along the straining direction, indicating that electron energy also varies monotonically from one end of the NW to the other [15] (Fig. 1a). The as-synthesized ZnO nanostructures are, however, intrinsically *n*-type doped with a typical donor concentration $\sim 10^{17}\,cm^{-3}$ [16]. Considering the statistical electron distribution, the electrical field distribution in a strained ZnO NW with moderate charge carrier

density can be calculated, indicating that free electrons tend to accumulate at the positive piezoelectric polarization side and partially screen the effect of the positive polarization charges at thermal equilibrium [17] (Fig. 1b), which is consistent with the experimental observation [18,19]. Recent efforts also demonstrate stable *p*-type doping is feasible for ZnO nanostructures due to the dislocation-free volume and the presence of high concentration of vacancies near the surface of the NWs [20—24]. With finite *p*-type doping, the holes tend to accumulate at the negative piezoelectric polarization side and partially screen the effect of the negative polarization charges at thermal equilibrium [20] (Fig. 1c).

## Piezotronic effect

Piezotronic effect describes the modulation of charge carrier transport across metal-semiconductor (M-S) barrier or *p—n* junction by mechanical deformation, which results from the redistribution of free carriers and alteration of band structure near the interface due to the existence of strain-induced polarization charges [8,9,12,25—27]. Electronic devices fabricated by utilizing these interfacial piezoelectric polarization charges as ''gate'' controlling signal is piezotronics, which is fundamentally different from electrically gated field effect transistor (FET). Intensive efforts have been devoted to derive analytical expressions for unveiling the underlying principle of piezotronics and the electromechanical properties of piezoelectric NWs have also been investigated in details [28,29]. The piezotronic effect in M-S contacts and *p—n* junctions is to be discussed in details and brief overview of the corresponding analytical results will be provided as well to facilitate quantitative understanding of the effect.

### Effect of piezoelectric polarization on M-S contact

M-S contact is a fundamental structure in semiconductor electronics and optoelectronics [30]. When metal and semiconductor come into contact, a significant redistribution of charge takes place due to the overlap of wave functions from both the metal and semiconductor [31,32]. The alignment of Fermi levels on either side of the interface results in a net charge transfer and an abrupt discontinuity or energy barrier is induced at the interface, which is the Schottky barrier with barrier height of $e\phi_{Bn}$. Schottky barrier height (SBH) is a measure of the mismatch of energy levels for majority carriers, which dictates the transport of charge carriers across M-S interface and is critical for operation of related semiconductor device. For Schottky barrier formed between piezoelectric semiconductor and metal, the strain-induced negative piezoelectric polarization charges induced at the semiconductor side near the barrier interface can repel the electrons away from the interface, resulting in further depleted interface and increased local barrier heights (Fig. 2a); while the positive piezoelectric polarization charges created at the semiconductor side can attract the electrons toward the interface, giving rise to less depleted/accumulated interface and hence decreased local barrier heights (Fig. 2b) [12,33]. The strain-induced polarization charges can hence directly affect the local contacts at the metal-semiconductor interfaces and the transport of charge carriers across the M-S contact by exerting substantial influences on the concentration/distribution of free carriers in semiconductors and on modulation of electronic charge in interface states or metal, depending on the crystallographic orientation of the piezoelectric semiconductor material and the polarity of the applied strain [9,12,8].

By ignoring the surface states and other anomalies, characteristics of M-S contact (i.e. space charges distribution, electric field and energy band) with the presence of piezoelectric polarization charges at thermal equilibrium are shown in Fig. 2. The strain-induced polarization charges at the interface change not only the SBH but also the width of depletion region. The carriers transport in M-S contact is dominated by the following expression [34],

$$J_n \approx J_D \cdot \left[\exp\left(\frac{qV}{kT}\right) - 1\right]$$

where $J_D v \approx q^2 D_n NC \cdot (kT)^{-1} \cdot \sqrt{[2qN_D(\psi_{bi} - V) \cdot \varepsilon_s^{-1}]} \cdot \exp[-q\phi_{Bn} \cdot (kT)^{-1}]$ is the saturation current density, $\varepsilon_s$ is the permittivity of the semiconductor material, $D_n$ is the diffusion coefficient for electrons, $N_C$ is the effective density of states in the conduction band and $N_D$ is the donor concentration in the semiconductor. The effect of piezoelectric charge can be considered as perturbation to the conduction-band edge and corresponding effective SBH is then derived as $\phi_{Bn} = \phi_{Bn0} - q^2 \rho_{piezo} W_{piezo}{}^2 (2\varepsilon_s)^{-1}$, where piezoelectric polarization charges distribute in the region with width of $W_{piezo}$ near the barrier interface, $\phi_{Bn0}$ is the SBH without the polarization charges [28]. The current density across the Schottky barrier can hence be rewritten as

$$J_n \approx J_{D0} \cdot \exp[q^2 \rho_{piezo} W_{piezo}^2 (2kT\varepsilon_s)^{-1}] \cdot \exp[qV \cdot (kT)^{-1} - 1].$$

where $J_{D0}$ is the saturation current density when no piezoelectric polarization charge is introduced. If the induced strain is $s_{33}$ along the *c*-axis of ZnO NW, the piezoelectric polarization can be obtained from $P_z = e_{33} s_{33} = q\rho_{piezo} W_{piezo}$, where $\rho_{piezo}$ represents the density of induced piezoelectric polarization charges. Consequently, the current density can be expressed as

$$J \approx J_{D0} \cdot \exp[qe_{33} s_{33} W_{piezo} \cdot (2kT\varepsilon_s)^{-1}] \cdot \exp[qV \cdot (kT)^{-1} - 1].$$

This manifests the dependence of current transported across the M-S interface on both the magnitude and polarity of induced strain, which is the fundamental mechanism of piezotronic devices such as strain-gated transistors [6,35,36].

### Effect of piezoelectric polarization on *p—n* junction

A *p—n* junction consists of two semiconductor materials with opposite doping type is another critical component in modern electronics and optoelectronics [37]. The inter-diffusion of holes/electrons when forming the junction creates the charge depletion zone which is void of mobile carriers. As per previous discussions, the presence of such a carrier depletion zone can significantly enhance the electrostatic

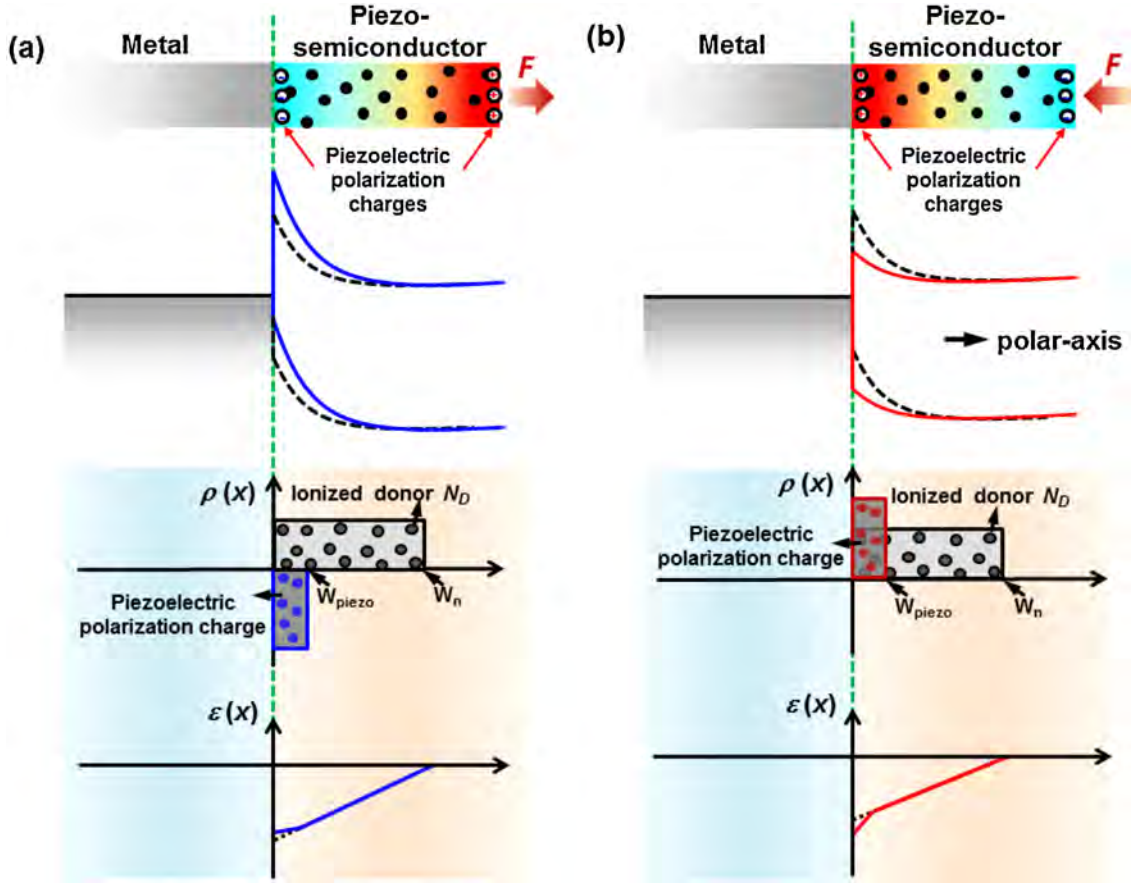


**Figure 2** Schematic of energy diagram, space charges distribution and electric field illustrating the effect of piezoelectric polarization on modulating the M-S contact characteristics. (a) With tensile strain applied, the negative piezoelectric polarization charges induced near the interface (symbols with ''−'') increases the local SBH. (b) With compressive strain applied, the positive piezoelectric polarization charges induced near the interface (symbols with ''+'') decreases the local SBH. The band diagrams for the M-S contact with and without the presence of piezoelectric charges are shown using solid and dashed curves, respectively. Black dots represent the free charge carriers in the bulk semiconductor.

effect of the piezoelectric polarization charges due to the negligible screening by regional residual free carriers [12]. For simplicity, the case for *p*—*n* homojunction with *n*-type material piezoelectric is discussed here (Fig. 3). The strain-induced positive piezoelectric polarization charges in the *n*-type region adjacent to the junction interface attract the negatively charged screening charges (e.g. electrons) toward the interface, resulting in the trapping or accumulation of electrons close to the interface and the downward bending in the local band profile (Fig. 3a) [12]. Conversely, the negative piezoelectric polarization charges created in the *n*-type region close to the junction interface can repel the electrons away from the interface, resulting in the depletion of electrons adjacent to the interface and the upward bending in the local band structure (Fig. 3b) [12]. To quantitatively understand this effect on the *I*—*V* characteristics of piezoelectric *p*—*n* junctions, an abrupt junction model is used here, in which the impurity concentration in a *p*—*n* junction changes abruptly from acceptor $N_A$ to donor $N_D$ [37]. The built-in potential is given by

$$\psi_{bi} = q \cdot (2\varepsilon_s)^{-1} \cdot (N_A W_{Dp}^2 + \rho_{piezo} W_{piezo}^2 + N_D W_{Dn}^2),$$

where $N_D(x)$ is the donor concentration, $N_A(x)$ is the acceptor concentration, $W_{Dp}$ and $W_{Dn}$ are the depletion layer widths in the *p*-side and the *n*-side, respectively [28]. This suggests that the change in built-in potential can be modulated by the strain-induced piezoelectric charges. For a simple case in which locally $p_{n0} \gg n_{p0}$, where $p_{n0}$ is the thermal equilibrium hole concentration in *n*-type semiconductor and $n_{p0}$ is the thermal equilibrium electron concentration in *p*-type semiconductor, the total current density of the *p*—*n* junction based piezotronic transistor is given by

$$J = J_{C0} \cdot \exp[q^2 \rho_{piezo} W_{piezo}^2 (2kT\varepsilon_s)^{-1}] \cdot \exp[qV \times (kT)^{-1} - 1],$$

where $J_{C0}$ is the saturation current density with the absence of piezoelectric polarization [28]. This shows that the current transported across the *p*—*n* junction depends on the density of strain-induced polarization charges as well as the polarity of applied strain. More complicated situations involving *p*—*n* heterojunctions can be discussed accordingly. Similar discussions can also be extended to cases including *p*-type piezoelectric semiconductor materials.

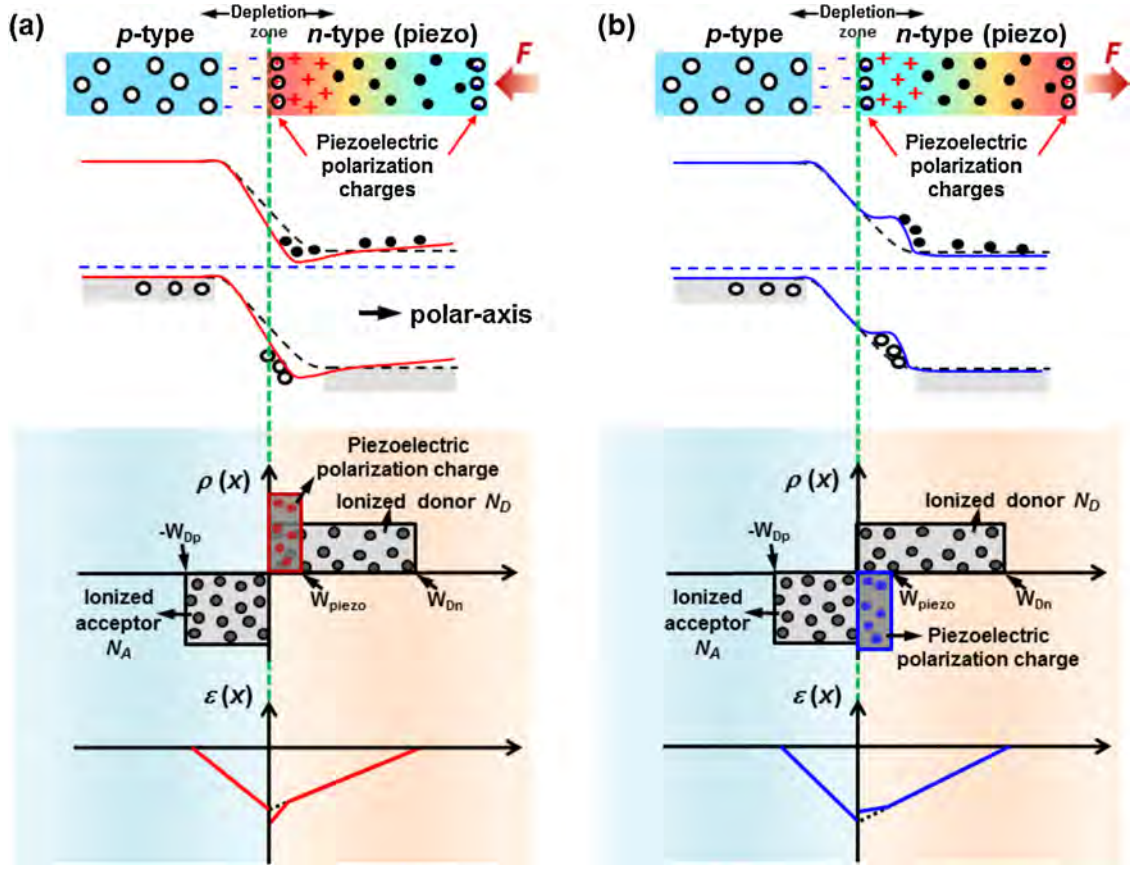


**Figure 3** Schematic of energy diagram, space charges distribution and electric field illustrating the effect of piezoelectric polarization on modulating the *p*—*n* junction characteristics. With strain applied, the piezoelectric polarization ionic charges are induced near the junction interface. The color gradients in (a) and (b) indicate the distribution of piezopotential, with red representing positive piezopotential and blue representing negative piezopotential. The band diagrams for the *p*—*n* junction with and without the presence of piezoelectric charges are shown using solid and dashed curves, respectively. Black dots and empty circles represent the free charge carriers in semiconductor. Symbols ''+'' and ''—'' represent the ionized donors and acceptors in respective regions. (For interpretation of the references to color in this figure legend, the reader is referred to the web version of the article.)

## Piezotronic device based on *n*-type nanomaterials

Mechanical straining of ZnO NWs can induce the piezoelectric polarization, which may act as the controlling signal for gating the charge carriers transport in piezotronic devices such as strain-gated electromechanical switch and diode [38—40]. Following these preliminary demonstrations, more complex functionalities have been subsequently achieved by coupling the piezoelectric polarization with electrical transport in semiconductors. The strain-induced polarization can also tune the sensitivity of Schottky-barrier based nanostructured sensors.

### Strain-gated piezotronic logic devices

By replacing the external gating voltage with the piezoelectric polarization charges for controlling the charge transport, the fundamental principle and implementation of two-terminal strain-gated piezotronic transistors have been presented [6,35,41]. The strain-induced polarization charges are also capable of modulating channel conductivity of electronics heterogeneous to the piezotronic device [42].

A strain-gated transistor (SGT) can be made of a single ZnO NW with its two ends being fixed by source and drain electrodes on a flexible substrate (Fig. 4a). The external mechanical perturbation induced strain ($\varepsilon_g$) acts as the gate input for controlling the ''on''/''off'' state of the NW SGT. The positive/negative strain is created when the NW is stretched/compressed. The $I_{DS}$—$\varepsilon_g$ curves at a fixed $V_{DS}$ show that $I_{DS}$ increases as the gate strain $\varepsilon_g$ increases and the threshold gate strain $\varepsilon_T$ is around 0.08% (Fig. 4b). An externally applied mechanical strain ($\varepsilon_g$) results in both the strain induced band structure change and piezoelectric polarization charges at reversely biased Schottky contact formed between ZnO NW and electrode. The change in band structure leads to the piezoresistive effect, which is non-polar and symmetric at both the source and drain contacts. Since ZnO is a polar structure along *c*-axis, straining in axial direction (*c*-axis) induces the polarization of cations and anions and the asymmetric modulations on the SBHs at the drain and source electrodes. As the strain $\varepsilon_g$ is swept from compressive to tensile regions, the $I_{DS}$ current can be effectively modulated from ''on'' to ''off''.

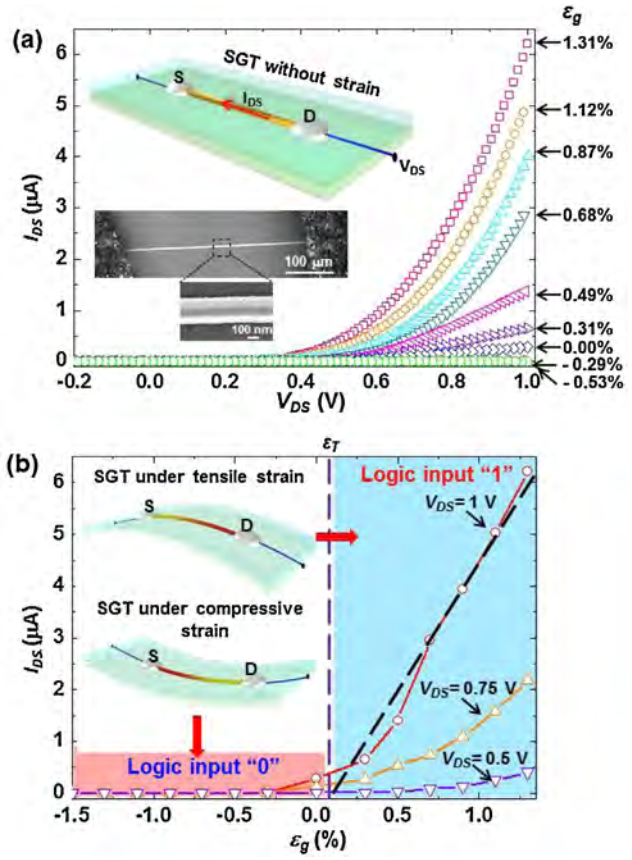


**Figure 4** Single ZnO NW strain-gated transistor (SGT). (a) $I_{DS}$—$V_{DS}$ output characteristic for a ZnO SGT device. (b) $I_{DS}$—$\varepsilon_g$ transfer characteristic for the same ZnO SGT device under three different $V_{DS}$ bias values: 1 V, 0.75 V and 0.5 V.
Reprinted with permission from [35]. Copyright 2010 WILEY-VCH Verlag GmbH & Co. KGaA, Weinheim.

A better illustration of the basic concept of piezotronics is shown in Fig. 5 by comparing SGT with conventional metal-oxide-semiconductor-field-effect transistor (MOSFET) [43]. Piezotronic strain-gated complementary logic gates can then be built by packaging two *n*-type ZnO NW SGTs on top and bottom surfaces of the same flexible substrate. Universal logic units such as inverters, NAND, NOR, XOR gates have been demonstrated for performing piezotronic logic calculations, which possess the potential for integration with MEMS technology to achieve advanced and complex functional actions [35]. More complex piezotronic computation such as one-bit binary addition by half-adder, which operates over the input mechanical strains with corresponding computation results provided in electrical domain, has recently been demonstrated using GaN nanobelt-based strain-gated piezotronic logic devices [43].

## Piezotronic electromechanical memories

The piezoelectrically modulated resistive switching device based on ZnO NW has been demonstrated utilizing piezotronic effect, through which the write/read access of the memory cell can be programmed via electromechanical modulation [34]. Adjusted by the piezoelectric polarization charges created at the semiconductor/metal interface under externally mechanical deformation, the resistive switching characteristics of the memory can be controllably modulated, and the logic levels of the mechanical strain can be recorded and read out electrically.

The external mechanical perturbation induced strain ($\varepsilon_g$) acts as the programming input for modulating the hysteretic *I*—*V* characteristics of the piezoelectrically modulated resistive memory (PRM) cell. When the PRM cell was tensile stretched ($\varepsilon$ = 1.17%), the hysteretic switching curve shifted toward lower voltage side by 1.49 V (red line in Fig. 6a); when the cell was compressively deformed ($\varepsilon$ = —0.76%), the hysteretic switching curve shifted toward higher voltage side by 1.18 V (blue line in Fig. 6a). $V_{th,S+}$, $V_{th,S0}$, $V_{th,S-}$ and $V_{th,D+}$, $V_{th,D0}$, $V_{th,D-}$ are the threshold switching voltages for the PRM cell under tensile, zero and compressive strains, respectively. The ratios of conductance between low resistance state (LRS) and high resistance state (HRS) for the PRM cell remain steady at high values ($\sim 10^5$) under different strains. The changes in threshold switching voltages of the PRM cell with different strains have been plotted in Fig. 6b. It can be seen that the change in both the $V_{th,S}$ and $V_{th,D}$ almost linearly depends on strain applied to the PRM cell, while the width of the HRS window ($V_{th,Si}$—$V_{th,Di}$, where $i$ = +0, —) remains almost constant for different strain values. The modulation effect of strain on the hysteric switching behavior of the PRM cell can then be explained using the band-diagram of the working device (Fig. 6c). If the PRM cell is under tensile strain with the Schottky barrier at drain side being forward-biased ($V > 0$ in Fig. 6a), the positive strain-induced polarization charges reduced the SBH at the reverse-biased source barrier; while the negative polarization charges increased the SBH at the forward-biased drain barrier (red line in Fig. 6c1). Since the *I*—*V* characteristic is dictated by the reversely biased source barrier, the existence of strain-induced piezoelectric polarization charges results in the shift of switching threshold voltage from $V_{th,S0}$ to $V_{th,S+}$, indicating only a smaller bias is required to switch the PRM cell from HRS to LRS state. Conversely, if the Schottky barrier at drain side is reverse-biased ($V < 0$ in Fig. 6a), the SBH is still reduced at the source barrier while it is increased at the drain barrier (Fig. 6c2) since the polarity of the strain did not change, and hence the piezoelectric polarization charges remained negative and positive at source and drain barriers, respectively. The *I*—*V* characteristic is now dictated by the reversely biased drain side in this case, and a shift of switching threshold voltage from $V_{th,D0}$ to $V_{th,D+}$ was observed, indicating a larger bias has to be applied in order to switch the PRM cell from HRS to LRS state. By the same token, in the case of applying a compressive strain to the PRM cell, the shift of switching threshold voltage from $V_{th,S0}$ to $V_{th,S-}$ and $V_{th,D0}$ to $V_{th,D-}$ can be explained. The PRM can further function as an electromechanical memory, in which the write/read access can be programmed via mechanical actuation. A pulse train consisting of several write/read/erase pulses is applied to the PRM cell to record and read out the logic levels of the strain in the cell, by monitoring the characteristic patterns in the output current. A quantitative analysis of the magnitudes of the output currents can give the absolute values of the strains stored in the PRM cells [44].

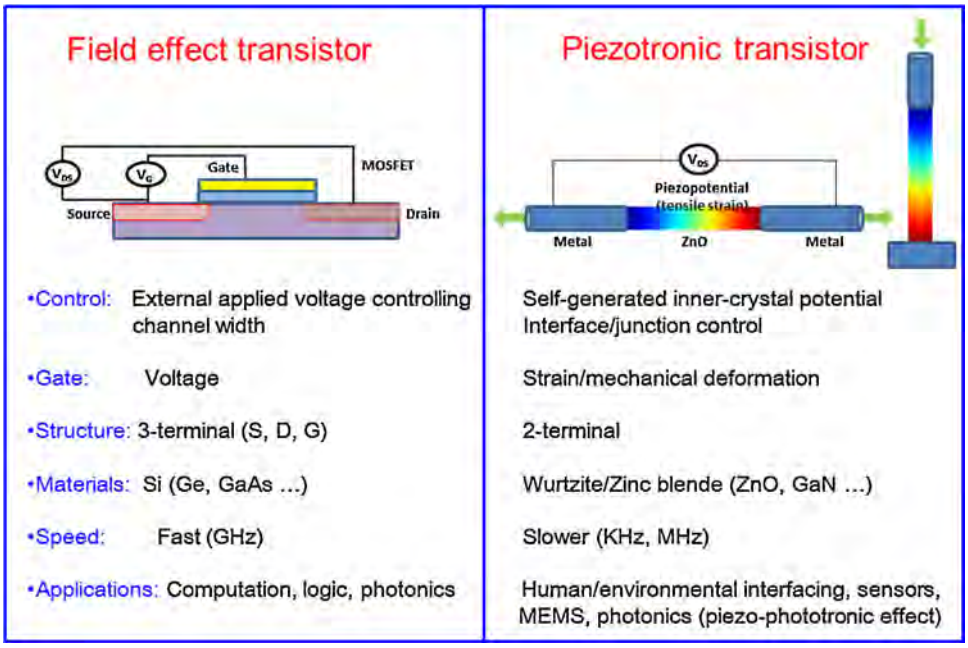


**Figure 5** Comparison between traditional FET and strain-gated transistor (SGT).
Reprinted with permission from [43]. Copyright 2013 American Chemical Society.

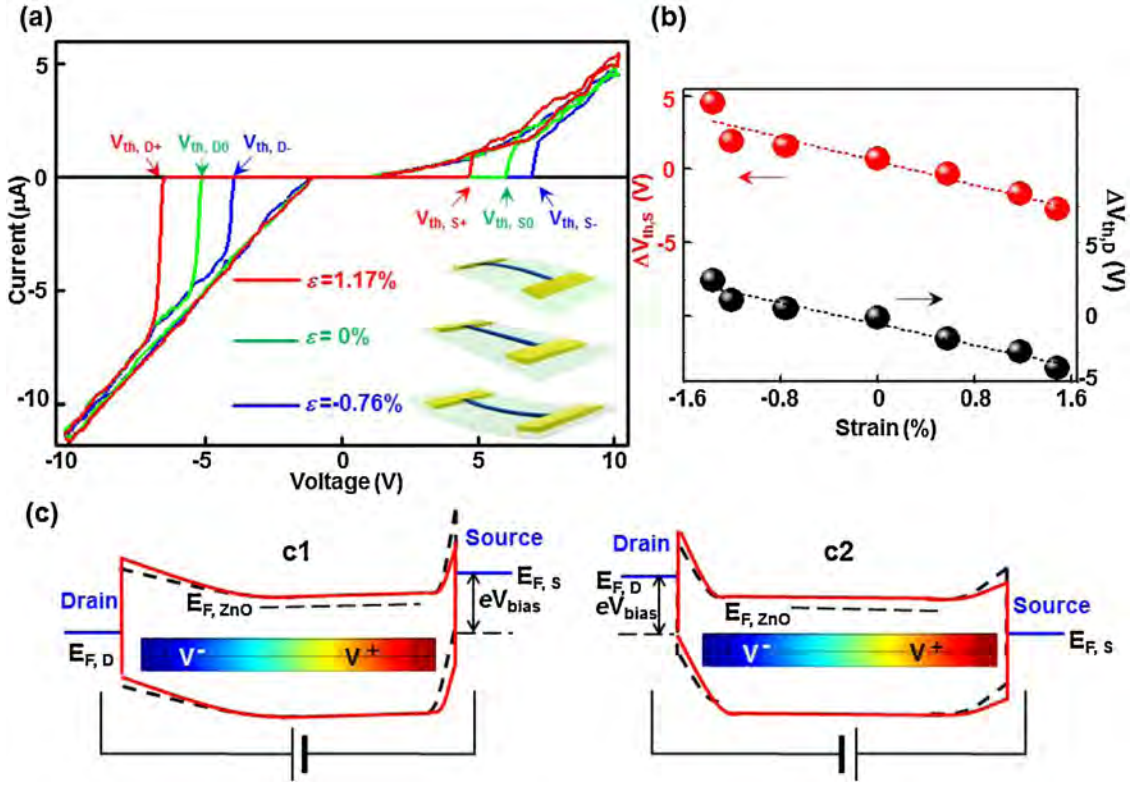


**Figure 6** Stain-modulated hysteretic switching of PRM cell. (a) *I*—*V* characteristics of ZnO PRM cells under tensile, zero and compressive strains respectively. (b) Dependence of threshold voltages on applied strains. (c) Schematic of band-diagram of PRM cell under tensile strain. (c1) Schottky barrier at drain side is forward biased. (c2) Schottky barrier at drain side is reversely biased. Red solid lines represent band-diagrams after tensile strain is applied. Black dashed lines represent band-diagrams under strain free condition. (For interpretation of the references to color in this figure legend, the reader is referred to the web version of the article.)
Reprinted with permission from [44]. Copyright 2011 American Chemical Society.

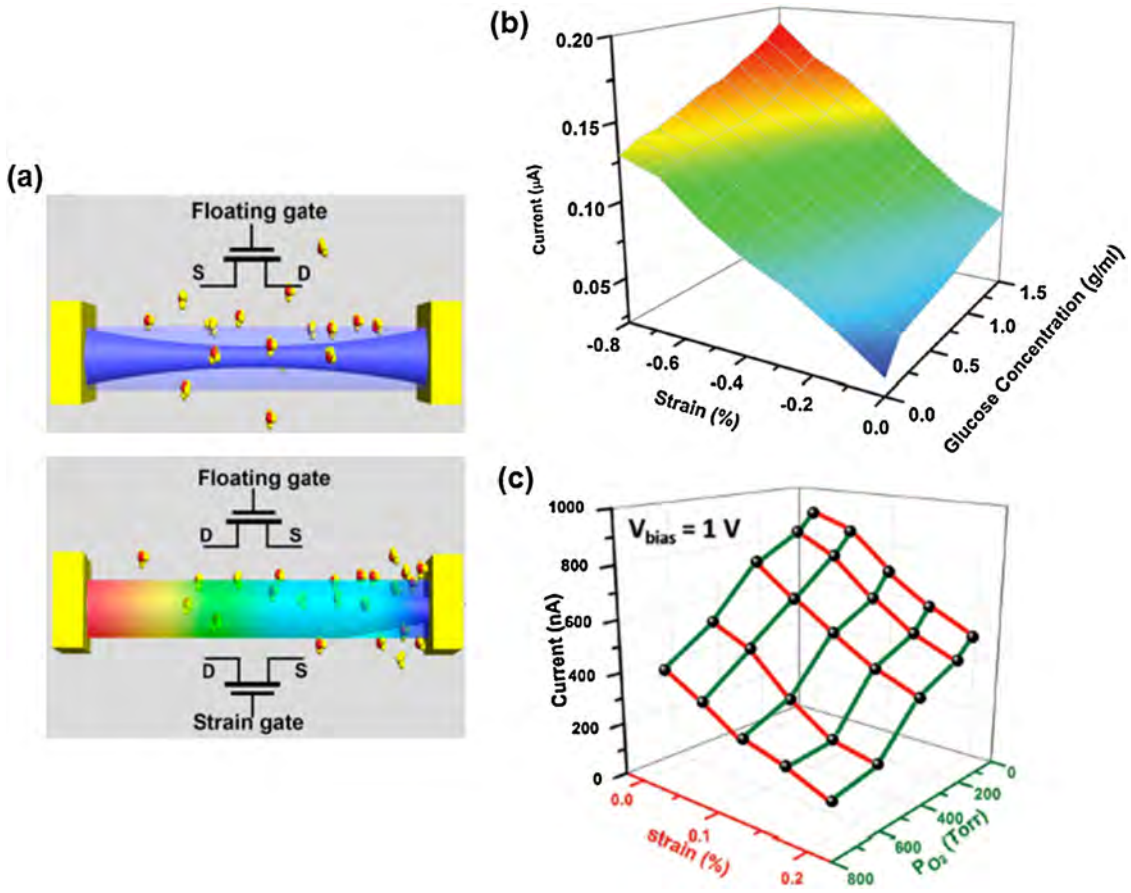


**Figure 7** (a) Top, working principle of the traditional NW sensor, which detects the species under the conrol of a ''floating gate'' introduced by the adsorption and desorption of the detected species. Bottom, working principle of the ZnO micro/nanowire Schottky-contacted sensor with the signal current enhanced by piezotronic effect. (Reprinted with permission from [49]. Copyright 2013 American Chemical Society). (b) 3D surface graph indicating the current response of the ZnO NW glucose sensor under different strains and glucose concentrations. (Reprinted with permission from [48]. Copyright 2013 WILEY-VCH Verlag GmbH & Co. KGaA, Weinheim.) (c) 3D graph depicting the current response of the ZnO NW oxygen sensor under different strains and oxygen pressures at a bias voltage equal to 1 V. (Reprinted with permission from [51]. Copyright 2013 WILEY-VCH Verlag GmbH & Co. KGaA, Weinheim).

## Biochemical and gas sensors enhanced by piezotronic effect

Schottky-contact based nanodevices have recently been utilized for ultra-violet (UV), gas, and biochemical sensing with enhanced sensitivity and improved response time compared to Ohmic-contact devices [45—47]. Unlike Ohmic-contacted sensors, in which the sensitivity is dictated by bulk channel modulation due to adsorbed species, Schottky-contacted sensors are implemented by tuning local SBH at interface via adsorption of surface charged/polar species (Fig. 7a). The sensitivity of the sensor relies on the optimization of SBH, because too large SBH blocks the current to flow through and hence renders the measurement difficult (e.g. low signal-to-noise ratio), while too small SBH makes the device insensitive to variation of adsorbed species. In devices built from piezoelectric semiconductors, the strain-induced polarization can also modulate the SBH at the local interface effectively [8,9]. It has been recently demonstrated that the sensitivity of the Schottky-contacted sensors can be modulated by piezoelectric polarization via the piezotronic effect [48—51]. The performance of the ZnO NW based glucose sensor was generally enhanced when applying a −0.79% compressive strain on the device, and the magnitude of the output signal was increased by more than 200%; the sensing resolution and sensitivity of sensors were improved by more than 200% and 300%, respectively (Fig. 7b) [48]. Similar principle has been applied to improve the performance of a ZnO NW protein sensor in which the sensitivity is increased by more than 50 times under compressive strain (approx. −0.82%). Furthermore, the piezoelectric polarization in the micro/nanowire leads to a non-uniform distribution of the target species (e.g. biomolecules and gas molecules) at the micro/nanowire surface owing to electrostatic interaction, which may further improve the detection limit of the sensors. Although gigantically enhanced performance has been achieved in Schottky-contact gas sensors [47], these sensors still need to work at elevated temperature (175—300 °C) which limits their utilizations in portable biomedical applications. The modulation and optimization of SBH via strain-induced polarization offers alternate approach for engineering sensing capability of NW based gas sensor at room temperature[51]. Under the positive bias, the relative current change at oxygen pressures from 16 to

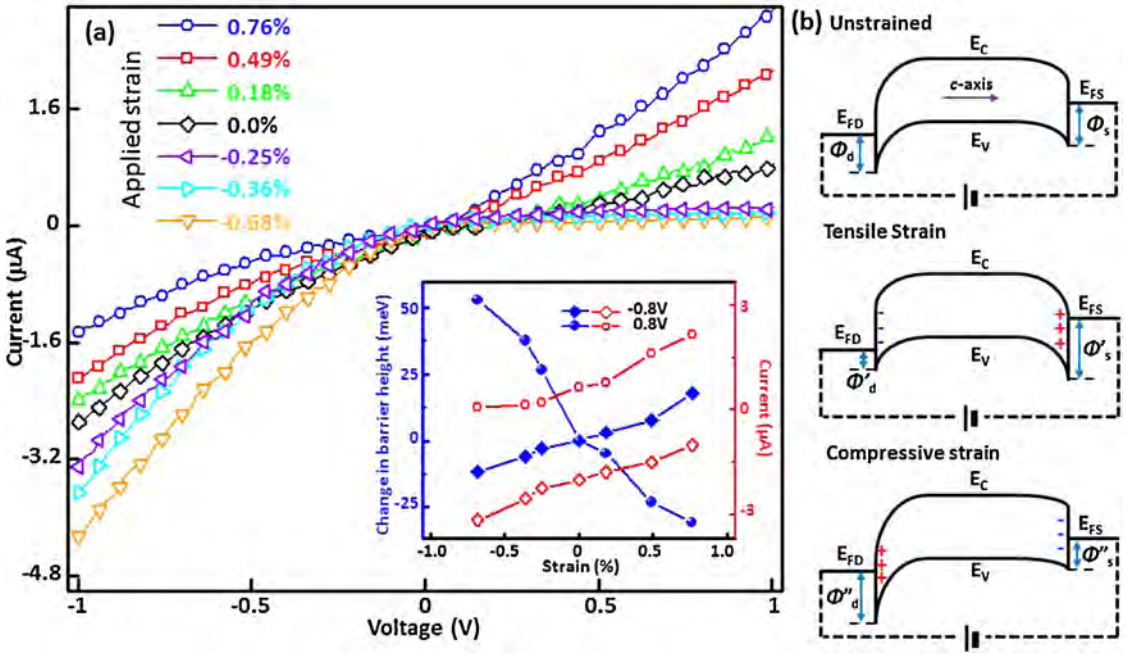


**Figure 8** Observation of the piezotronic effect in a 0.2% Sb doped NWs. (a) *I*—*V* curves of the wire under different levels of strain show modulation of device conductivity by mechanical strain. Inset shows the measured current and calculated change in Schottky barrier height as a function of strain at two fixed drain biases. (b) Positive drain bias on the NW causes the source and drain quasi-Fermi levels ($E_{FS}$ and $E_{FD}$) to shift based on the level of the applied voltage. Tensile strain will induce negative piezoelectric polarization charges (blue ''—'') near the interface of drain contact, attracting free holes, lowering the local Schottky barrier height, and increasing current. Compressive strain will induce positive piezoelectric polarization charges (red ''+'') near the interface of the drain contact, depleting free holes, increasing the local Schottky barrier height, and decreasing current. (For interpretation of the references to color in this figure legend, the reader is referred to the web version of the article.)
Reprinted with permission from [23]. Copyright 2013 American Chemical Society.

700 Torr enhances from −55.4% to −75.4%, respectively, as the applied tensile strain increases from 0 to 0.2% (Fig. 7c). Under the negative bias, the relative current change at oxygen pressures from 16 to 700 Torr increases from −87.3% to −93%, respectively, as the applied tensile strain increases from 0 to 0.2%. This enhancement of sensitivity is mainly due to the changed SBH by piezoelectric polarization. The principle shown here can also be extended to other sensing applications for improving the sensitivity, sensing resolution and the performance.

## Piezotronic device based on *p*-type nanomaterials

Almost all the existing piezotronic devices were fabricated using intrinsically *n*-type ZnO and few studies of piezotronics based on *p*-type materials, especially *p*-type ZnO, have been done. In order to develop a full understanding of the piezotronics theory and enable novel piezotronic applications in electronics and optoelectronics, it is essential to investigate the feasibility of *p*-type piezoelectric semiconductors for piezotronics.

The successful growth of ultra-long Sb-doped *p*-type ZnO NWs was recently demonstrated using a low-temperature solution growth method [23]. Electrical transport measurement confirmed clear *p*-type characteristics for both 0.2% and 1% Sb-doped ZnO NWs. The electrical transport characteristic of 0.2% doped sample was re-measured after two months, demonstrating stable *p*-type behavior. The first *p*-type ZnO NWs based piezotronic transistors were then developed, which extends the concept of piezotronics and its potential applications in flexible electronics and optoelectronics. *I*—*V* characterization of the as-fabricated two-terminal device was obtained when the device was subject to different strains. Corresponding results shown in Fig. 8a indicate that transport properties of the devices can be modulated by the applied mechanical strain. The polarity of the applied bias is with respect to drain electrode. For positive drain bias, the current through the device increased under tensile strain, and decreased with compressive strain. Conversely, under negative drain bias, the current increased under compressive strain and decreased with increased tension. The ''gating'' effect of external strain on charge carrier transport in *p*-type ZnO NW piezotronic devices is demonstrated more explicitly in the inset of Fig. 8a. The corresponding strain-induced change in SBH demonstrates a change of 53 meV in SBH at drain contact with an applied compressive strain of 0.68%. The band diagrams of *p*-type ZnO NW piezotronic device are shown in Fig. 8b to better explain the underlying working mechanism. For the case of positive drain bias (Fig. 8b), the drain contact is reversely biased, so $\Delta\Phi_d$ dictates the charge carrier transport. When tensile strain is applied to the device, negative piezoelectric polarization charges are induced at the drain contact. If the doping level inside the NW is finite, these immobile

ionic charges will only be partially screened and can attract the majority charge carriers (i.e. holes) toward the M-S interface, which decreases the SBH at the drain contact ($\Phi'_d < \Phi_d$). At the same time, positive piezoelectric polarization charges are induced at the source contact, which results in an increased SBH at the source contact ($\Phi'_s > \Phi_s$). When compressive strain is applied to the device, on the other hand, positive piezoelectric polarization charges are induced at the drain contact, which depletes holes near the M-S interface and increases the SBH at drain contact ($\Phi''_d > \Phi_d$). Simultaneously, negative piezoelectric polarization charges are induced at source contact, lowering the SBH at source contact ($\Phi''_s < \Phi_s$). This leads to the observed *I*—*V* curves shown here, in which the applied mechanical strain functions as the controlling gate signal to modulate the carrier transport in *p*-type ZnO NWs based piezotronic transistors.

## Piezotronic effect in thin films based structures

Although 1D nanostructures are promising building blocks for future electronics, technical difficulties in implementing 1D nanostructures based devices hinder their immediate applications. Despite the numerous techniques reported for bottom-up synthesis of 1D semiconductor nanostructures [52—56], the lack of uniformity in as-synthesized materials, in terms of dimensions, morphologies and doping levels, leads to performance inconsistency from device to device. Moreover, the techniques currently available for positioning, aligning and integrating as-synthesized 1D nanostructures are either cumbersome or incompatible with state-of-art microfabrication technologies. Specifically for piezotronic applications, determination and engineering control of the polar axis orientation in as-synthesized nanomaterials, which still remains elusive, is of pivotal importance for further integration. On the other hand, piezotronic effect is prospected to be a pervasive effect [8] and also exists in various semiconductor nanomaterials such as GaN, $ZnSnO_3$ and CdS [41,57—61]. Moreover, the success of semiconductor technology is enabled by thin-film processing that provides engineering control over material properties as well as scalable integrated fabrication processes. Investigating and utilizing piezotronic effect in thin film based material systems can hence potentially circumvent the limitations posed by 1D nanostructures and fully appreciate the state-of-art microfabrication technologies.

The first attempt to investigate piezotronic effect in RF-sputtered ZnO thin films was recently performed [62]. ZnO thin film with controllable property was grown via RF sputtering on flexible substrates. The characterization result indicates that ⟨0 0 0 1⟩, corresponding to the *c*-axis of wurtzite ZnO, is the preferred growth direction and suggests that the as-grown film consists of multiple mesoscopic columnar grains. The alignment of the *c*-axes within these columnar grains gives rise to macroscopically observed piezoelectricity of the ZnO polycrystalline thin film. Piezoelectric tests were performed to determine the polarity of the film and it is found that properties of the substrates are crucial in dictating the piezoelectric polarity of the RF-sputtered ZnO thin film [62]. To explicitly

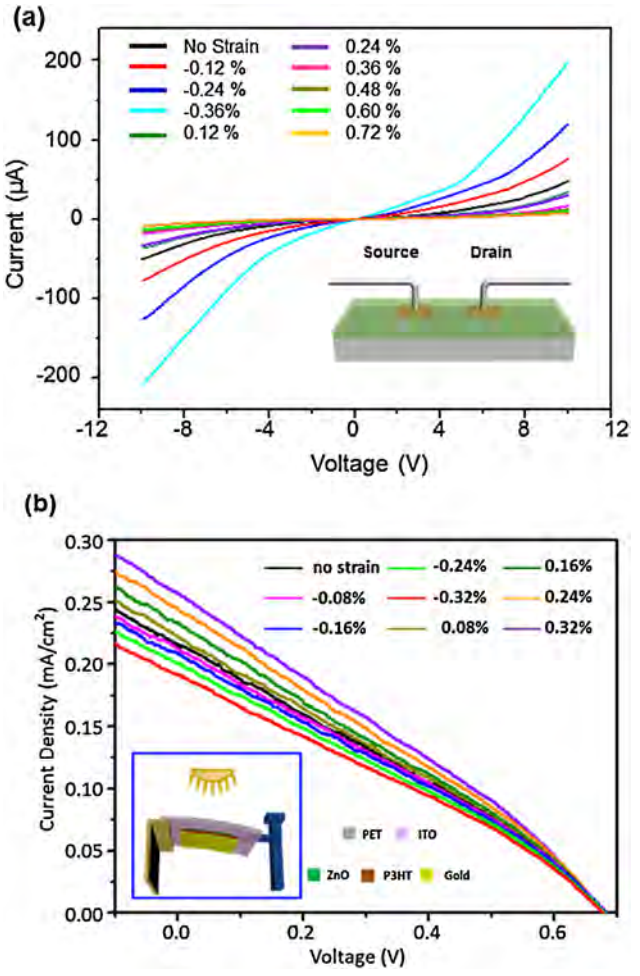


**Figure 9** (a) *I*—*V* curves under different strains were obtained from a thin-film piezotronic device with Schottky contact electrodes. (Reprinted with permission from [62]. Copyright 2013 WILEY-VCH Verlag GmbH & Co. KGaA, Weinheim.) (b) Strain-modulated photovoltaic performance of ZnO thin film/P3HT hybrid solar cell.
Reprinted from [63], with permission from Elsevier. Copyright 2013 Elsevier Ltd.

demonstrate the ''*gating*'' effect of external strain on modulating the charge carrier transport in ZnO thin film piezotronic device, current values (*I*) in device under various strains were monitored at fixed bias. $I_0$ was the current flowing through the device when no strain was applied. The conductivity of the entire thin film device is dictated by the reversely biased contact and the effective conductivity of the device is sensitive to the change in SBH at that specific contact. Different from previous piezotronic devices based on 1D nanomaterials in which metal-semiconductor contacts are formed at the two opposite polar surfaces, both source and drain electrodes in the ZnO thin film piezotronic devices are in contact with the same surface of as-deposited ZnO film, and hence piezoelectric polarization charges with same polarity will be induced at both Schottky contacts when external strain is applied. This leads to the observed *I*—*V* curves (Fig. 9a) in which same modulation trend of applied strain on conductivity can be observed when either source or drain side is reversely biased. As pointed out

earlier, this may help circumvent the difficult and elusive predetermination of *c*-axis orientation for 1D nanostructures and significantly simplify the further integration. It is also demonstrated that UV sensing capability of as-fabricated thin film based piezotronic device can be tuned by piezoelectric polarization charges, showing significantly enhanced sensitivity and improved reset time under tensile strain [62]. More recently, the influence of strain-induced polarization in thin-film ZnO/P3HT solar cell system has been investigated in details study, showing that the overall solar cell performance can be controllably tuned by varying the applied strain (Fig. 9b) [63]. Considering the technological compatibility, piezoelectric semiconductor thin films could be the excellent alternative to 1D counterpart for realizing piezotronic applications. and broadening the scope of piezotronics to extend its potential applications in sensors [38,49,50,57—59], electronics [35,36,44], optoelectronics [60,61,63—69] and human—machine interfacing [6].

## System integration of large-scale array piezotronic devices

The rapid advancement in micro/nanotechnology is gradually shifting the focus from demonstrating discrete devices to developing integrated system of certain complexity via state-of-art micro/nano-fabrication technologies. Designing, fabricating and integrating arrays of nanodevices into a functional system is the key for transferring nano-scale science into applicable nanotechnology. In the following section, we will review the recent breakthroughs in system integration of large-scale array piezotronic devices for applications in strain/pressure imaging and human-electronics interfacing.

### 3D vertical nanowire piezotronic transistors array for active/adaptive interfacing

The large-array three-dimensional (3D) circuitry integration of piezotronic transistors based on vertical ZnO NWs as active taxel-addressable pressure/force-sensor matrix for tactile imaging has been recently reported [6], presenting the promises in implementing self-powered artificial skin for active/adaptive interfacing in applications such as human-machine interfacing, prosthetic devices, novel surgical instruments and biomedical therapy/treatments. The demand for restoring mobility and independence from the growing population of amputees and paralyzed people such as wounded soldiers, accident victims and diabetes drives the technological advance and bolsters the prosthetics market growth. It is reported that 1.9 million people live in the U.S. with limb loss, a number that is expected to double by 2050, and the total amount of amputations performed in the U.S. each year is 185,000 [70]. In all the incidences, patients suffer most from the loss of touch sense. Restoring touch sensation via electronic means, which is of pivotal importance, has nevertheless been challenging in prosthetics and biomedical therapy/treatment. Unlike other senses, touch sensing capability of human skin remains stubbornly difficult to be mimicked, which necessitates the development of large-scale pressure sensor arrays with high spatial-resolution, high-sensitivity, fast response and conformability. Current efforts utilize electrically controlled components like traditional planar field-effect-transistors (FETs) as read-out elements for passively detecting pressure-induced property change in pressure-sensitive media [71—75]. Efforts are devoted to minimize effect of substrate strain on performance of these electronic components while preserving the deformability of the substrate. This scheme of pressure sensing not only requires complicated system integration of heterogeneous components, but also lacks direct and active interfacing between electronics and mechanical actuations. Moreover, the sizes of as-fabricated taxels (tactile pixels) are of hundreds of microns to even tens of millimeters, severely limiting device density and spatial resolution. Although novel architectures like three-dimensional (3D) integrated circuits and wrap-gate vertical transistor present the attractive approaches to achieve high-density assembly of functional nanodevices [76—79], it is cumbersome to fabricate the gate electrode and manage interconnect layout for effectively controlling individual device within a high-density matrix (schematic of a representative wrap-gate NW FET is shown in Fig. 10a(left)). These existing prosthetic skins cannot provide sensory feedback either. Therefore, new approaches have to be developed for better mimicking or even competing with the tactile sensing capabilities of human skins for more capable prosthetics.

To overcome the limitations of existing artificial skins and address the increasing needs for adaptive/active prostheses, 3D array integration of vertical ZnO NW transistors circuitry ($92 \times 92$ taxels in $1\,cm^2$ with 234 taxels per inch) as flexible taxel-addressable force/pressure-sensor matrix for artificial skin was designed and developed [6]. Using the piezoelectric polarization charges created at M-S interface under strain to gate/modulate transport process of local charge carriers, piezotronic effect has been applied to design independently addressable two-terminal transistor arrays, which convert mechanical stimuli applied on the devices into local electronic controlling signals. The elimination of wrap gate offers a new approach for 3D structuring. The basic structure of a 3D strain-gated vertical piezotronic transistor (SGVPT) is depicted in Fig. 10a(right), consisting of one or multiple vertically grown ZnO NWs in contact with bottom and top electrodes on flexible substrates. ZnO NW experiences axial strain when subjected to external mechanical deformation, with piezopotential induced inside the NW due to polarization of non-mobile ions distributed at the two ends [8,9]. The local contact profile and carrier transport characteristics across the Schottky barrier, formed between ZnO NW and metal electrodes, is effectively controlled by the polarization-charge-induced potential. Electrical characteristics of the two-terminal SGVPT are therefore modulated by external mechanical actions induced strain, which essentially functions as a gate signal for controlling SGVPT (Fig. 10b). By combining the patterned in-place growth of vertically aligned ZnO NWs with state-of-the-art microfabrication techniques, large-scale integration of SGVPT array can be obtained. Fig. 10b illustrates the schematic of the SGVPT array with taxel density of $92 \times 92$ in $1\,cm^2$ (234 taxels per inch (TPI)). The equivalent circuit diagram of the SGVPT array is displayed in Fig. 10c to demonstrate the operation scheme of the SGVPT devices circuitry. The taxel area density of SGVPT

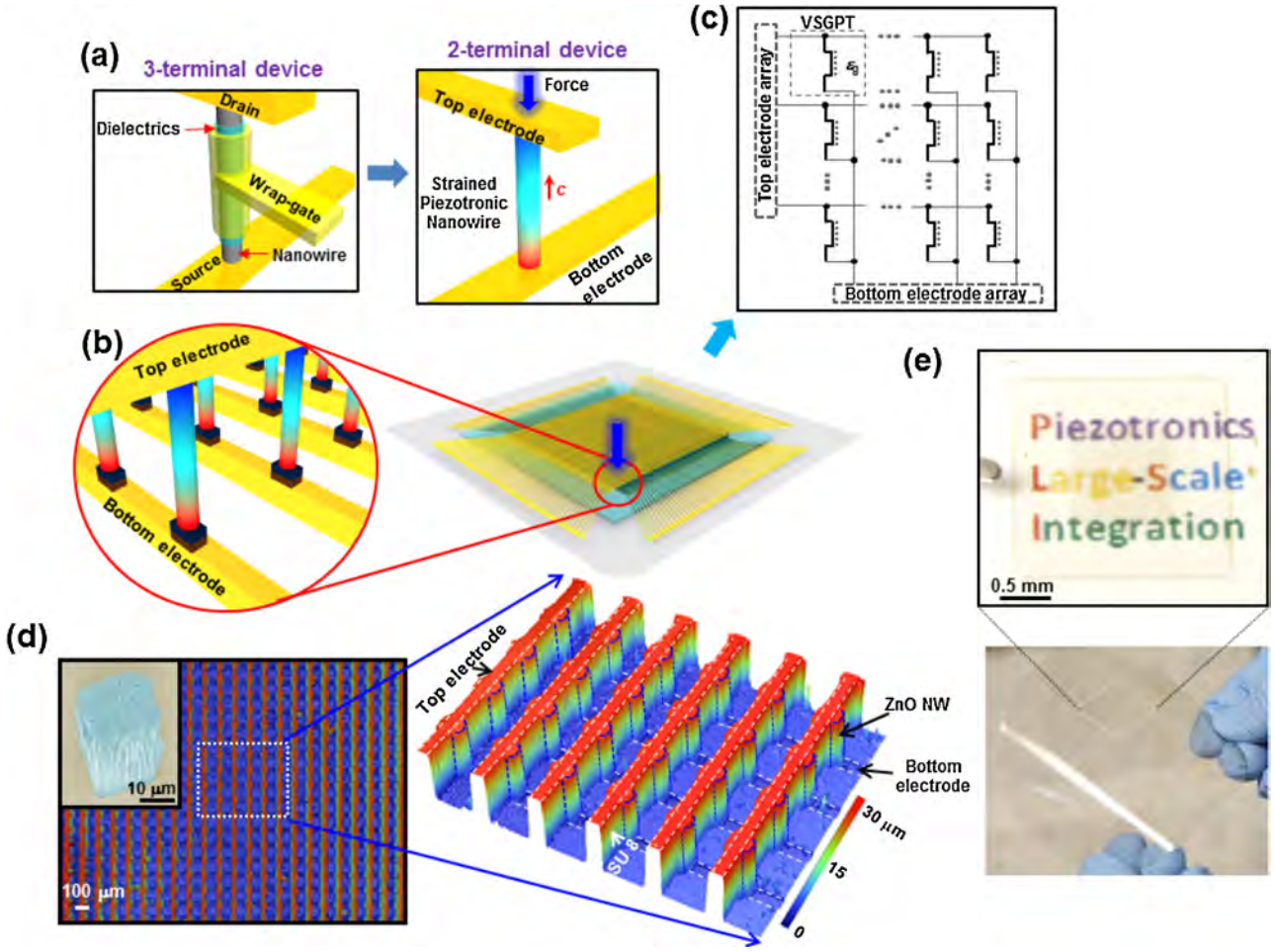


**Figure 10** (a) Comparison between three-terminal voltage-gated NW FET (left) and two-terminal strain-gated vertical piezotronic transistor (right). ZnO NWs in SGVPT grow along the *c* axis, as indicated by the red arrow. (b) Schematic illustration of a 3D SGVPT array with taxel density of 92 × 92 and scheme for spatial profile imaging of local stress (indicated by the downwards blue arrowhead) by the array (zoom-in schematic). (c) Equivalent circuit diagram of the 3D SGVPT array. The region highlighted by black dashed lines is the unit SGVPT device, in which $\varepsilon_g$ represents the mechanical strain gate signal and the vertical dotted line between the two terminals of SGVPT presents the modulation effect of $\varepsilon_g$ on the conducting characteristics of the device. (d) Topological profile image of the SGVPT array (top view). Inset, 3D perspective view of the topological profile image reveals the vertical hierarchy of the SGVPT assembly in which the color gradient represents different heights. (e) Transparency and flexibility of SGVPT array device. (For interpretation of the references to color in this figure legend, the reader is referred to the web version of the article.) Reprinted with permission from [6]. Copyright 2013 the American Association for the Advancement of Science.

array is 8464 $cm^{-2}$, which is higher than the number of tactile sensors in recent reports (~6–27 $cm^{-2}$) [71–73,80] and mechanoreceptors embedded in the human fingertip skins (~240 $cm^{-2}$) [81]. A detailed description of the device fabrication process is elaborated in Ref [6]. Briefly, the active array of SGVPTs is sandwiched between the top and bottom Indium Tin Oxide (ITO) electrodes, which are aligned in orthogonal cross-bar configurations. A thin layer of Au is deposited between the top/bottom surfaces of ZnO NWs and top/bottom ITO electrodes, respectively, forming Schottky contacts with ZnO NWs. A thin layer of Parylene C (1 μm thickness) is conformally coated on the SGVPT device as the moisture/corrosion barrier. Well-aligned ZnO NWs, synthesized by a low-temperature hydrothermal method [52], function as the active channel material of SGVPT and help reduce the stochastic taxel-to-taxel variation to ensure uniform device performance Fig. 10d(inset) shows the SGVPT after etching-back the SU 8 layer and exposing top portions (~20 μm) of the ZnO NWs. The as-synthesized ZnO NWs show single-crystallinity. The three-dimensional nature and vertical hierarchy of the SGVPT assembly is revealed by topological profile imaging (Fig. 10d) using an optical noncontact profilometer, which measures the phase change of light reflected from various heights in the structure by interferometry. The high degree in alignment and uniformity of SGVPT array in three dimensions (~30 μm in height and 20 μm × 20 μm in taxel size) is enabled by process control in both the bottom-up synthesis of NWs and top-down fabrication of circuitry. The use of a two-terminal configuration based on piezotronic effect simplifies the layout design and circuitry fabrication while maintains effective control over individual devices. Transparency and

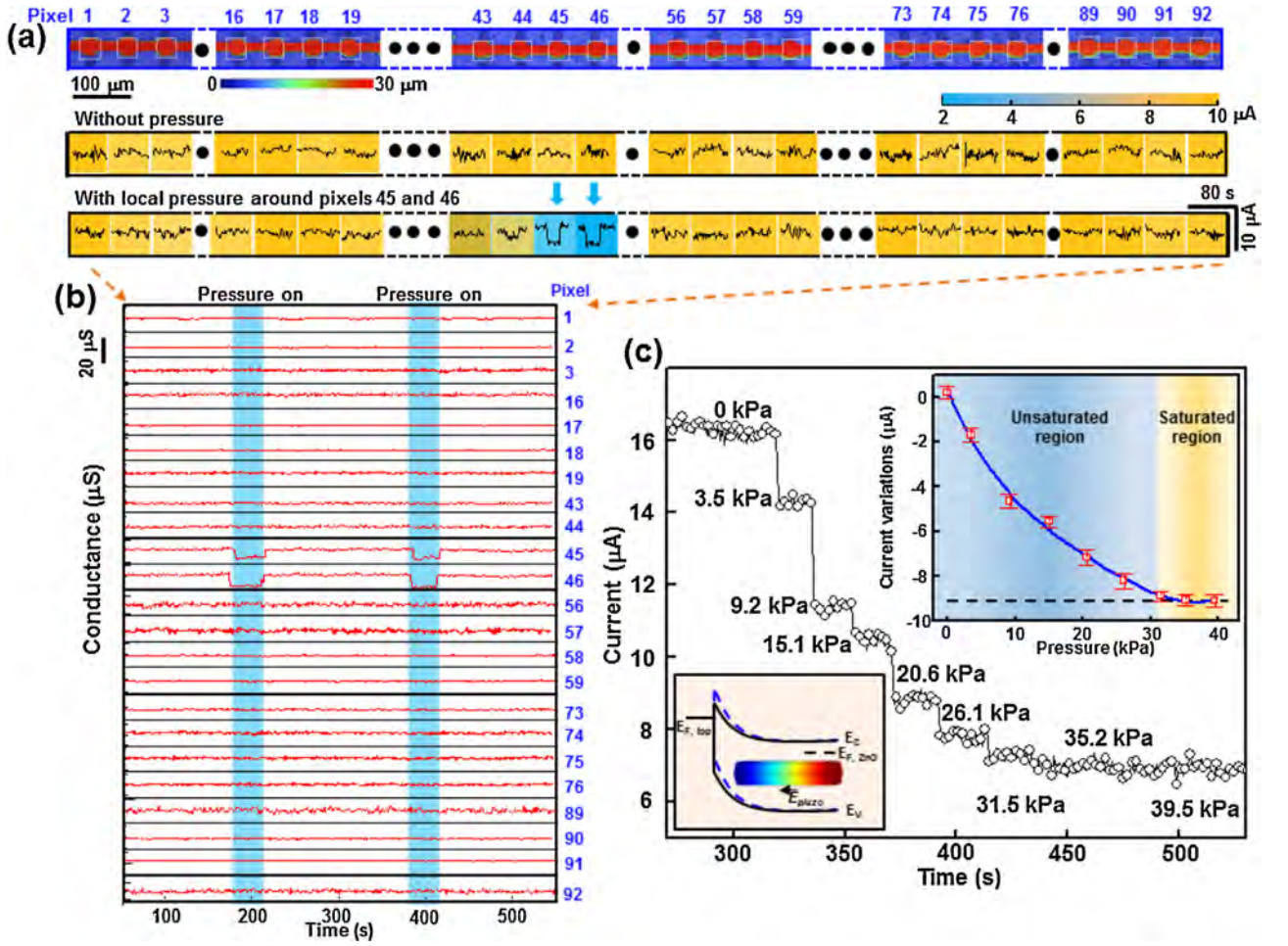


**Figure 11** (a) Topological profile images (top view) of 23 selected taxels in a 1 × 92 SGVPT array (single channel) (top frame) and their corresponding current responses (middle and bottom frames) under 1 V bias with and without external stress (20 kPa) applied to certain localized region (around taxels 45 and 46). (b) Single-channel conductance measurement in temporal domain illustrating the dynamic response of the 23 selected SGVPT devices in this channel, with and without pressure applied. (c) Current responses for taxel 46 under different pressures, presenting the gate modulation effect of applied pressure on the electrical characteristics of SGVPT. Top right inset, current variations (red squares) are plotted versus the applied pressures, clearly showing the saturation of current change when applied pressure is above ~30 kPa. Bottom left inset, schematic band-diagram illustrating the change in Schottky barrier height of the reversed biased top contact due to the modulation effect of strain-induced piezopotential. Color gradient represents the distribution of piezopotential field, in which red indicates the positive piezopotential and blue indicates the negative piezopotential. The original band-edges at the reversed biased Schottky contact for the SGVPT device without stress applied are shown in the black solid lines. The band-edges bending at the reversed biased Schottky contact for the SGVPT device with stress applied are shown in the blue dashed lines. (For interpretation of the references to color in this figure legend, the reader is referred to the web version of the article.)
Reprinted with permission from [6]. Copyright 2013 the American Association for the Advancement of Science.

flexibility of SGVPT array devices are also demonstrated (Fig. 10e).

Cross-bar electrodes have been configured for multiplexed data acquisition and spatial profiles of applied stress can be imaged. The output signal is current response so that it is easy to integrate SGVPT array with back-end interface circuits for fast data processing. Representative data from 23 taxels in a typical single-channel line-scan (1 × 92) measurement is shown in Fig. 11. The corresponding topological profile images (top view) of the selected taxels are displayed at the top of Fig. 11a. Current response from each taxel under 1 V bias, with and without external pressure (20 kPa) applied to a localized region (around taxels 45 and 46), is recorded. Dynamic response show distinctive conductance changes for taxels before and after applying the pressure (Fig. 11b). Although the measured response time (rise time) of ~0.15 s for SGVPT taxel is larger than that of human fingertips (~30–50 ms) [6], it is comparable to previously reported values of 0.1 s [71]. These results indicate that SGVPT array can respond to both static and some dynamic stimuli. The response time can be further improved in future design by integrating local on-site signal-processing circuits with SGVPT array [82]. It can be seen that for this single-channel array of SGVPTs, pressure variations can be

distinguished with both high sensitivity and spatial resolution (taxel periodicity ~100 μm). The dominant mechanism for the transport property of SGVPT is piezotronic effect rather than piezoresistive effect, as experimentally confirmed and elaborated in details [6]. From the measured variations in current responses by consecutively increasing the pressure load applied at fixed location, the SGVPT device demonstrates high sensitivity for detecting pressure change, particularly in low-pressure regions (<10 kPa). The modulation effect of applied pressure is shown from the plot of current variations against pressure changes (Fig. 11c) and the observed sensing range of a few kPa to ~30 kPa for SGVPT array is well matched to the 10—40 kPa range which a human finger applies to sense texture and shape [83]. The sensitivity for SGVPT, defined as $S = dG_{SGVPT}/dP$, is around 2.1 μS kPa$^{-1}$, which arises from the change in carrier transport of the SGVPT by applied pressure due to corresponding modulation of barrier height at the reversed biased Schottky contact by strain-induced piezopotential [8,9,28]. The conductance of SGVPT device is dictated by the reversed biased Schottky contact, which is formed between ZnO NWs and top electrodes in this case. Upon applying the normal stress, negative piezoelectric polarization charges induced at the reversed biased top Schottky contact raise the barrier height at that contact and hence decrease the transport conductance of the SGVPT taxel. The operation of SGVPT device is therefore based on barrier-interface-modulation that enables enhanced sensitivity and efficiency compared to the channel-modulation operation in conventional FETs. The quality of the Schottky contacts has been characterized as well [6]. The SBHs and ideality factors of the formed contacts for devices without extra oxygen plasma treatment before depositing the top electrode are $0.419 \pm 0.011$ eV and $5.84 \pm 1.29$ respectively, while the SBHs and ideality factors of the formed contacts for devices with extra oxygen plasma treatment before depositing the top electrode are found to be $0.575 \pm 0.013$ eV and $2.17 \pm 0.33$ respectively, indicating that the qualities of as-fabricated Schottky contacts have been improved by the oxygen plasma treatment [44].

The successful fabrication of the $92 \times 92$-taxel SGVPT array enables a 15—25-fold increase in number of taxels and 300—1000-fold increase in taxel area density compared to recent reports [71—73]. The output current of each individual SGVPT taxel is measured and averaged within a short duration window of 10 ms. By monitoring the output current of each independently functioning SGVPT taxel, spatial profile of applied pressure can be imaged by multiplexed-addressing all of the taxels. Metrology mapping performed without applying pressure demonstrates good uniformity in electrical characteristics among all of the taxels, with all of the 8464 SGVPTs within the array functioning and 95% of the SGVPTs possessing current values in the narrow range of $13.7 \pm 2.73$ μA under 1 V bias (Fig. 12a). Fig. 12b presents the difference between current values for each taxel before and after applying the normal stress, confirming that profile of applied stress can be spatially imaged. SGVPT devices are still operational and capable of imaging the spatial profile of applied pressure after 24-h immersion in 23 °C DI water and 37 °C 0.9% saline solution as well as after 6-h immersion in 65 °C DI water and 65 °C 0.9% saline solution, indicating the good stability and feasibility of SGVPT array operation for future applications like in vivo physiological sensing in complex environments [6].

The device matrix has also been demonstrated for achieving multi-dimensional active sensing, which demonstrate the potential of utilizing SGVPT array for future applications such as multi-dimensional signature recognition by not only recording the calligraphy or signature patterns, when people write, but also registering the corresponding pressure/force applied at each location/taxel and writing speed by the person. Normal stresses with well-determined values as well as spatial locations are applied to the device using the 3-axis stage and force gauge. The first group of six normal local stresses, each around 8.1 kPa, are applied to the array at pre-programmed locations in the sequence indexed from 1 to 6, with the corresponding contours imaged and organized, as shown in Fig. 12c1, to emulate the writing calligraphy of letter ''A'' (outlined by the white dashed lines). This process is achieved by varying the *x* and *y* coordinates while keeping the *z* coordinate constant in the control interface of the 3-axis stage. It can be seen that spatial profiles of all of the six applied stresses can be distinguished and mapped electronically. The second group of six normal stresses with the same locations are subsequently applied to the array in the same sequence, except that the stresses applied at sites 2 and 3 are increased to ~20 kPa with stresses at the rest four sites unchanged. The corresponding mapped contours are again recorded and organized, as shown in Fig. 12c2. This augmented capability can essentially provide means for realizing personal signature recognition with unique identity and enhanced security.

The SGVPT array has also shown capability of shape-adaptive high-resolution tactile imaging. The real time detection of shape changes caused by stretching or twisting is a desirable feature for sensors embedded in an artificial tissue or prosthetic device. A rectangular supporting object is fixed to the platen of probe station, directly beneath the central region of SGVPT array (Fig. 13). After the probe pins are in contact with the pads at the peripheral of SGVPT devices, the platen is further raised up so that SGVPT device is hunched by the underneath supporting object (Fig. 13, bottom) with the radius of curvature ~79.63 mm. The measured difference in taxel currents with and without the underneath supporting object is mapped and plotted in Fig. 13b1, illustrating a good agreement between the detected shape change of SGVPT array (dark blue regions) and the physical shape of the supporting object beneath the SGVPT device (outlined by white dashed lines). The shape-adaptive sensing capability is further examined by applying an additional localized stress to the bent SGVPT array, using the same setup in Fig. 12, as depicted by the 3D schematic drawing in Fig. 13b (bottom right). The measured variations in taxel current values between bent SGVPT array with extra stress and unstrained SGVPT array is imaged and plotted in Fig. 13b2. A clearer demonstration of the data can be obtained by numerically subtracting Fig. 13b1 from Fig. 13b2, which gives rise to spatial imaging of the additionally applied stress when the shape of the SGVPT device changes (Fig. 13b2—b1). Such shape-adaptive sensing has also been investigated for other radii of curvatures [6]. Because of the relatively large thickness of the SGVPT device (mainly contributed by the PET substrate which is 500 μm thick), the saturation of SGVPT response

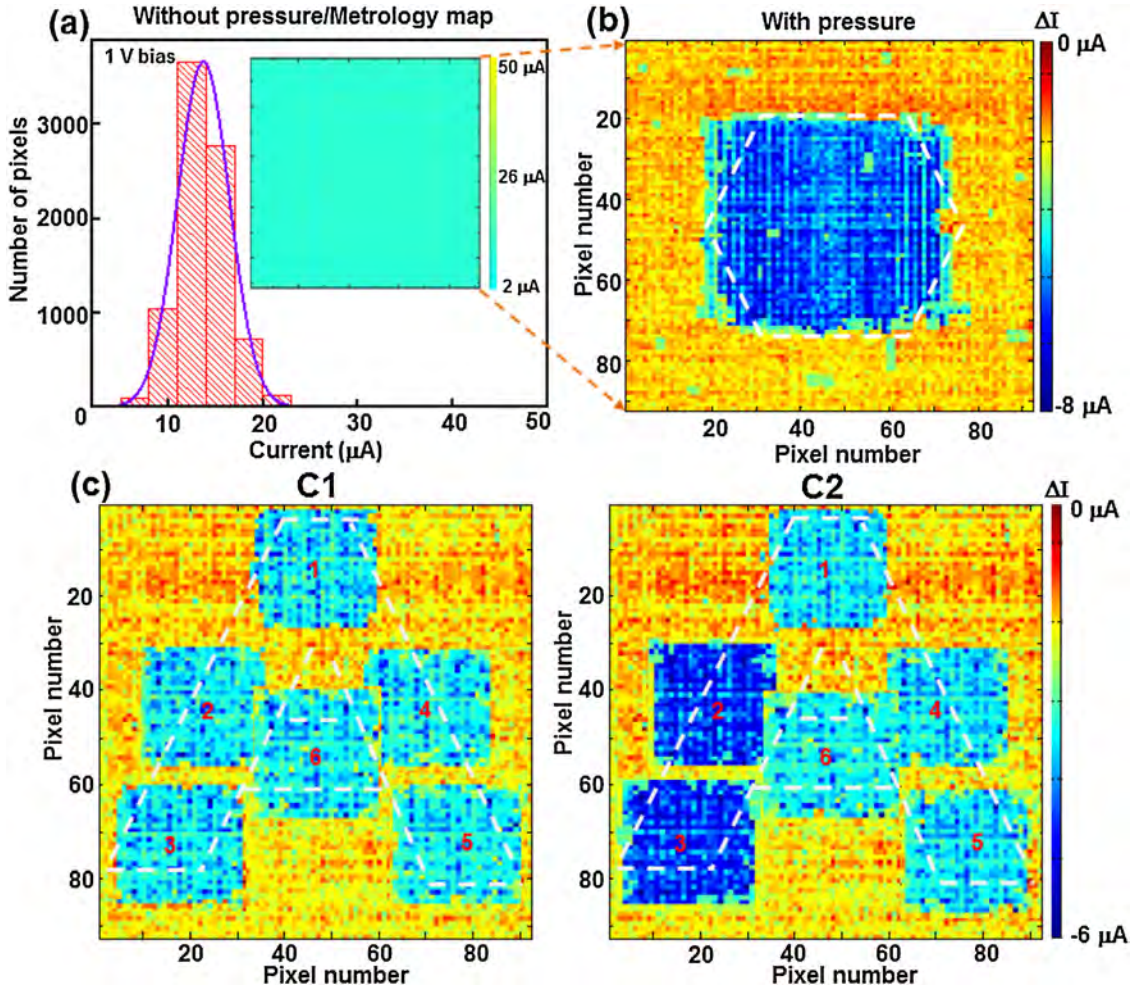


**Figure 12** (a) Metrology mapping (inset) and statistic investigation of the fully integrated SGVPT array without applying stress. (b) Current responses contour plot illustrating the capability of SGVPT array for imaging the spatial profile of applied stress. Color bar represents the current differences for each taxel before and after applying the normal stress. The physical shape of the applied stress is highlighted by the white dashed lines. (c) Multi-dimensional sensing by SGVPT array exhibits the potential of realizing applications like personal signature recognition with maximum security and unique identity. The calligraphy of written letter ''A'' is highlighted by the white dashed lines.
Reprinted with permission from [6]. Copyright 2013 the American Association for the Advancement of Science.

under large pressure (as shown in Fig. 11c) and the constraints of measurement set up (probes on probe card have limited movement in vertical direction), the SGVPT array is unable to sense the change in device shape and further distinguish the applied pressure when radii of curvature is smaller than 30—35 mm (Fig. 13c). The detectable range of shape deformation as well as corresponding shape-adaptive sensing can be improved by engineering the device into more compliant form to reduce the strain induced in SGVPT due to change in device shape. Cyclic bending has been further performed on SGVPT array for investigating the reliability and stability of device operations. In order to accelerate the aging process, SGVPT array has been repeatedly bent to a very small radius of curvature (15 mm) with 2-Hz cycle frequency. Metrology mapping has then been performed on SGVPT array and plotted for comparison with that of device before the cyclic bending. No significant degradation can be observed in operation of SGVPT array even after 1000-cycle bending, suggesting good stability in device operation.

Moreover, the SGVPT devices can also function as self-powered active tactile sensors by converting mechanical stimulations into electrical signals utilizing the piezopotential without applied bias, which emulates the physiological operations of mechanoreceptors in biological entities, such as human hair follicles and hair cells in the cochlea. The above technology is the first instance demonstrating 3D array integration of vertical NW piezotronic transistors for active/adaptive tactile imaging. It is also by far the largest 3D array integration of functional nanomaterials for artificial skin by combining the bottom-up synthesis of nanomaterials with state-of-art top-down micro-fabrications. The technology of 3D piezotronic transistor array offers immediate opportunities to meet needs from research, consumer and clinical sectors (e.g. in the fast-growing prosthetics market). The SGVPT array based technology for the

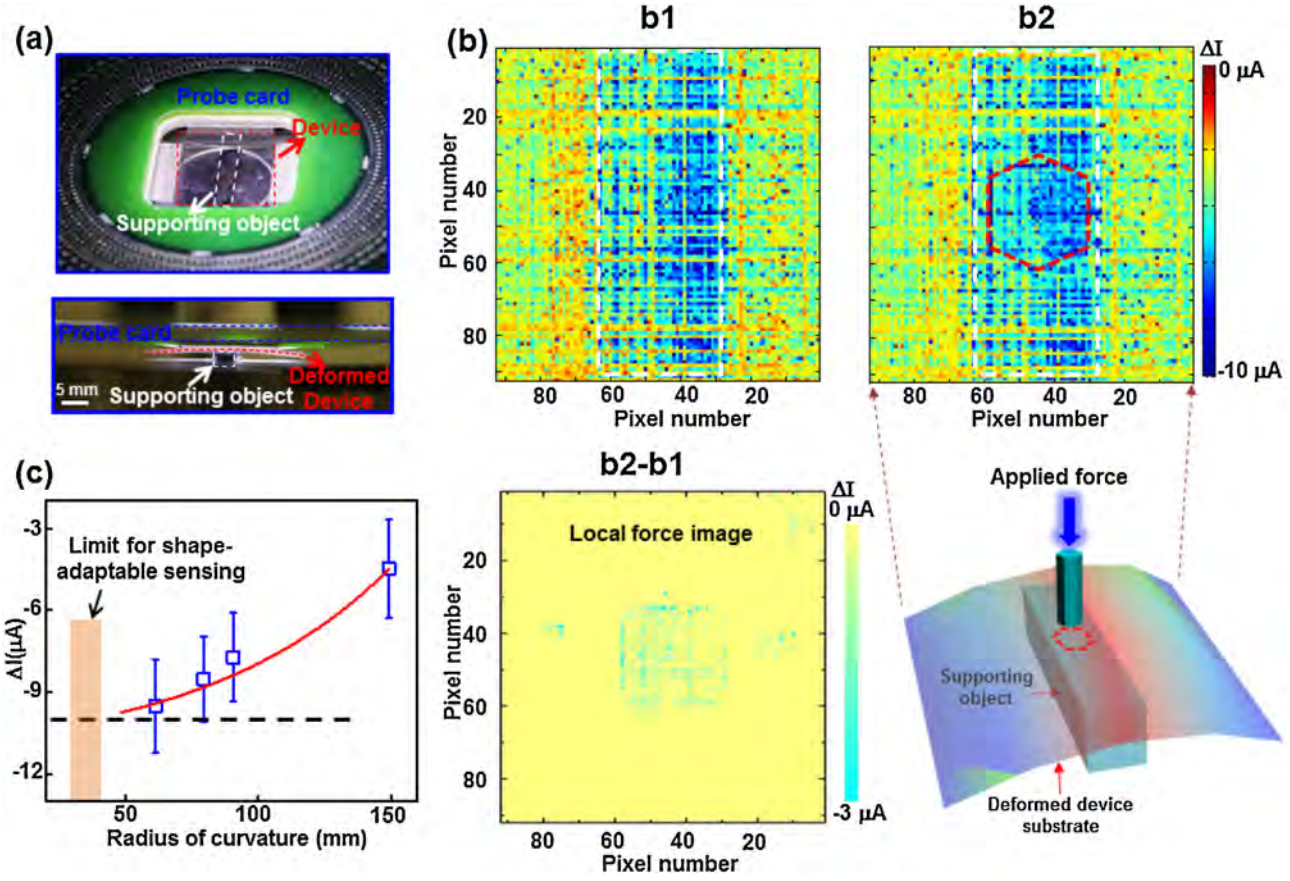


**Figure 13** (a) Optical photographs of the experimental setup for investigating the feasibility of SGVPT array for shape-adaptive sensing. The top one is the top view of the setup. The bottom one is the side-view of the setup, with the device deformed. (b) Shape-adaptive sensing of the SGVPT array. (b1) The measured difference in taxel currents for SGVPT array with and without underneath supporting object. The detected shape change of SGVPT array is illustrated by the dark blue regions and the physical shape of the supporting object beneath the SGVPT device is outlined by the white dashed lines. (b2) The measured variations in taxel current values between bent SGVPT array with extra stress and unstrained SGVPT array. The location/shape of the extra stress is outlined by the red dashed lines. (b2—b1) A clearer demonstration of the data is obtained by numerically subtracting Fig. 4b1 from Fig. 4b2, giving rise to spatial imaging of the additionally applied stress when the shape of the SGVPT device is changed. The 3D schematic drawing at the bottom right illustrates the process for shape-adaptive sensing. (c) Experimental results showing the limit for shape-adaptable sensing by SGVPT array with current design. (For interpretation of the references to color in this figure legend, the reader is referred to the web version of the article.)
Reprinted with permission from [6]. Copyright 2013 the American Association for the Advancement of Science.

first time allows us to directly control large-scale functional electronics by mechanical stimulations and enables the active/adaptive interfacing between electronics and ambient. These capabilities emerge directly from the uniqueness of the technology in ways that are impossible with existing approaches. It also exhibits the potential to be integrated with silicon-based CMOS technology and hence its potential and impact is broad.

## Piezoelectric NW LED array for electroluminescent imaging of pressure distribution

The piezoelectric polarization charges can also tune/control the charge separation, transport and/or recombination in optoelectronic processes [9,25,8], which has been used to enhance the performance of photocells [63,66,69,84—86], the sensitivity of photodetectors [87—90] and the external efficiency of an LED [64,67]. It has been recently demonstrated that strain-controlled LED emission can be used to fabricate a rapidly responding, optically based pixel array of strain sensors to directly 'image' the force/pressure distribution on the device at a resolution of only a few micrometers [91]. The design principle makes use of strain-induced polarization charges to tune the local light-emitting intensity of individual NW-LEDs. The two-dimensional intensity distribution then becomes a map of the pressure distribution on the surface.

The device was based on a patterned array of *n*-ZnO NWs grown on a *p*-GaN thin-film substrate, with the *c*-axis pointing upwards from the film (Fig. 14a) [52], forming an array of pixelled light emitters. Details about the fabrication of this LED array device can be found in Ref. [91]. Briefly, The NWs were fabricated by combining photolithography patterning

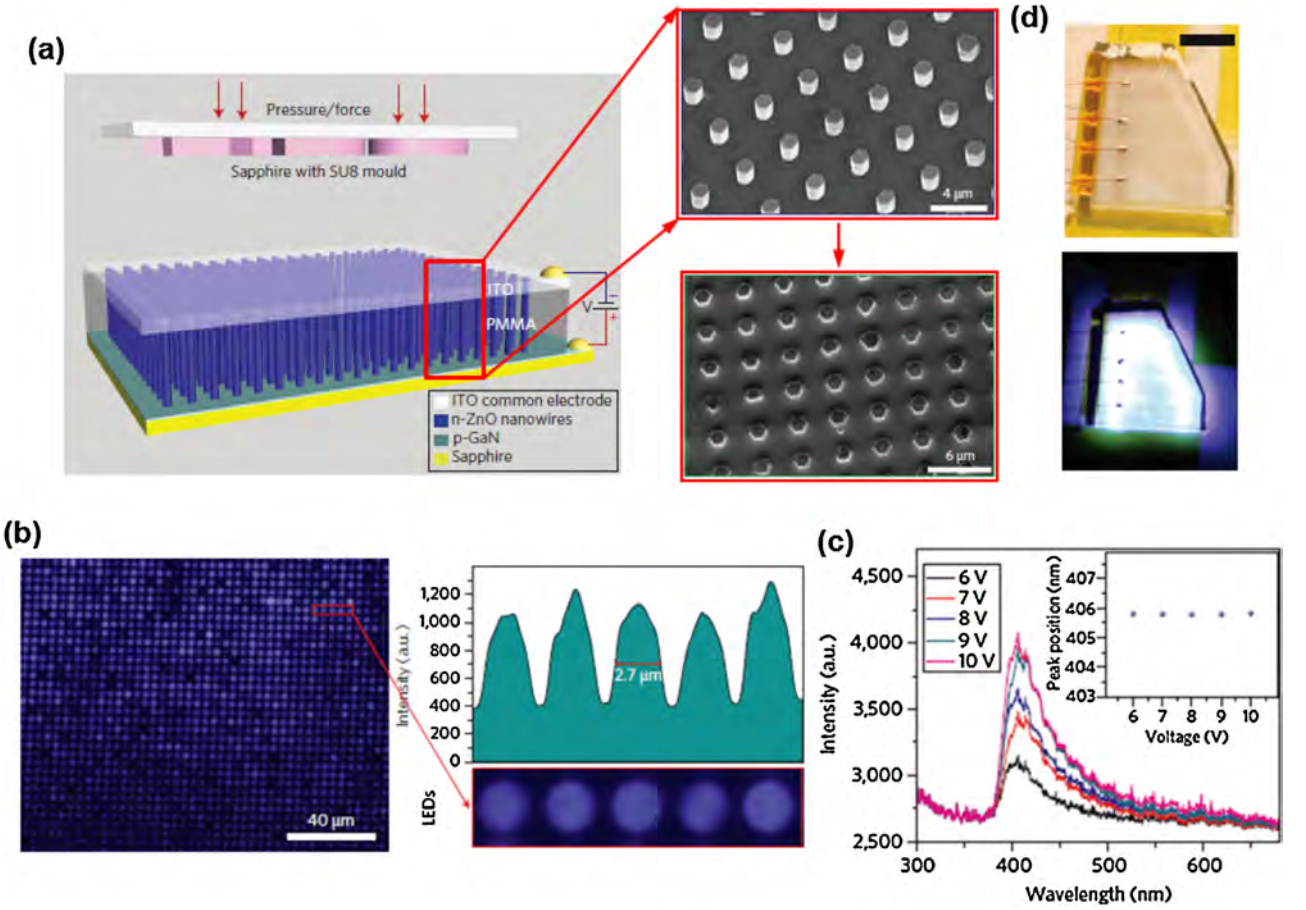


**Figure 14** (a) Design of the NW-LED-based pressure sensor array before applying a compressive strain. Insets: top, SEM images of the as-grown ZnO NW arrays on the *p*-GaN film; bottom: an ITO layer is deposited as a common electrode on top of the *n*-ZnO NWs. (b) Optical image of a NW-LED array when electrically emitting light. Insets: Five typical NW LEDs (marked with a red rectangle in a) and a corresponding line profile of the emission intensity from which the possible spatial resolution achieved by the sensor can be estimated. (c) Corresponding optical spectra of emitted light at bias voltages of 6, 7, 8, 9 and 10 V. Inset: dependence of peak position on applied voltage. (d) Optical image of a fabricated device and corresponding image when the device was electrically lit up at a bias voltage of 5 V, showing blue-white light emission from the NW-LED array. Scale bar is 5 mm. (For interpretation of the references to color in this figure legend, the reader is referred to the web version of the article.)
Reprinted with permission from [91]. Copyright 2013 Nature Publishing Group.

and low-temperature wet chemical growth. Ordered arrays of vertical *n*-type ZnO NWs were fabricated by uniform epitaxial growth on a *p*-GaN film to form the basic pixels of the sensors (Fig. 14a, inset). Scanning electron microscopy (SEM) images clearly show that all the NWs are wrapped by PMMA, and that the heads of the nanowires are exposed following oxygen plasma etching (Fig. 14a, inset). A Ni/Au electrode was used to form Ohmic contact with the bottom *p*-GaN, and an ITO layer was deposited in direct contact with the ZnO NWs on top, thereby serving as common electrodes for the entire NW array. The NW-LED array can be uniformly lit up under a bias of 5 V. An optical image of a lit LED array is shown in Fig. 14b, where each MW is a single light emitter and also a pixel unit. The center-to-center distance between two adjacent spots is 4 μm, corresponding to a pixel resolution of 6350 dpi. Five typical NW-LEDs marked with a red rectangle in Fig. 14b are enlarged and displayed together with their intensity line profile. There is little crosstalk between adjacent pixels, and the actual resolution is 2.7 μm, as defined by the full-width at half maximum (FWHM) of the emission pixels. The emission spectra obtained at different bias voltages (6, 7, 8, 9, 10 V) at room temperature are shown in Fig. 14c. Electroluminescence intensity increases with an increase in bias voltage, as expected from the band-bending model of a *p*—*n* junction. The major emission peak located at 406 nm is identified as violet-blue emission, which can be associated with the interface emission [92] and does not show any obvious shift when the bias voltage is increased. Corresponding image when the device was electrically lit up at a bias voltage of 5 V shows blue-white light emission from the NW-LED array (Fig. 14d).

Straining the basic unit cell of ZnO results in polarization of the cations and anions in the crystal because of its non-centrally symmetric structure. A schematic band diagram of a *p*-GaN/*n*-ZnO *p*—*n* junction composed of NW-LEDs, as shown in Fig. 15a, can be used to illustrate the piezotronic effect on the device before (black line) and after (red line) applying a strain. When the ZnO NW is under compressive

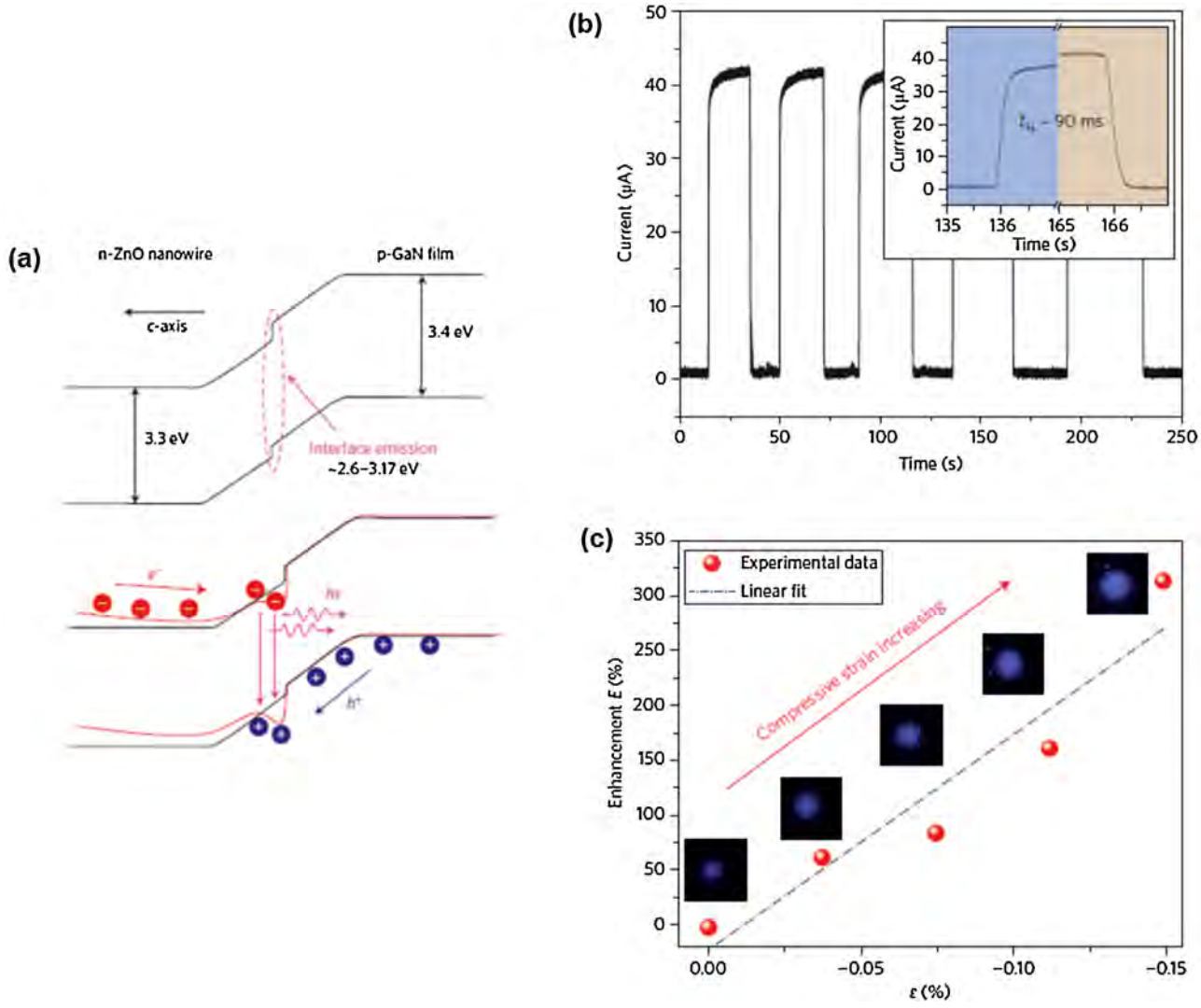


**Figure 15** (a) Schematic band diagram of a *p*-GaN/*n*-ZnO *p*—*n* junction before (black line) and after (red line) applying a compressive strain, where the dip created at the interface is due to the non-mobile, positive ionic charges. (b) Fast response and recovery of the NW-LED pressure sensors. Inset: enlarged image of one cycle, showing response and recovery times of ~90 ms. (c) Enhancement factor E of a NW-LED as a function of an applied compressive strain of up to −0.15%, together with the corresponding emitting light images. (For interpretation of the references to color in this figure legend, the reader is referred to the web version of the article.)



strain, the strain inside the NW is much larger than that in the GaN film because of the low coverage of NWs on the substrate surface (small contact cross-section), so a piezopotential is created in the NW. If the c-axis of the ZnO NWs is pointing away from the GaN film, the presence of the non-mobile, positive ionic charges at the *p*—*n* junction region may result in a local dip in the band if the concentration of free carriers is low within the charge-depletion zone of the junction. The distorted band tends to temporarily trap holes near the GaN—ZnO interface, increasing the carrier injection rates toward the junction region, and increasing the recombination rate of electrons and holes. Furthermore, the presence of the piezopotential along the NW is equivalent to applying an extra forward-biased voltage on the device. The depletion width and internal field are therefore reduced, and the injection current and emitting light intensity subsequently increased, when the device is compressed [8,9,12]. The results are supported by a theory proposed in relation to the photon emission at a *p*—*n* junction in the presence of local piezoelectric charges. In this theoretical work, analytical results under simplified conditions are presented with the aim of understanding the core physics of the piezotronic devices, and numerical models are developed to illustrate the photon emission process and the carrier transport characteristics of a practical example of the piezoelectric LED [93]. Under forward bias, the light emitting intensity of the NWs under compressive strain is increased significantly, while the remaining NWs under no strain show barely any change in electroluminescence intensity. Based on the intensity change of the emitting

nano-LEDs, the pressure/strain distribution across the entire array can be mapped at a resolution of a few micrometers. This is the principle of our sensor array.

The NW-LED pressure sensor has a fast response and fast recovery. Fig. 15b shows current versus time for five cycles of applied pressure. Response an relaxation times of less than 0.1 s were measured, which was largely determined by the period of time needed to apply/retract the mechanical force. Indeed, the true response of our device is expected to be much faster than 0.1 s. The emission intensity of a single-pixel NW-LED can be largely tuned/controlled by the magnitude of the applied strain. An image taken by a charge-coupled device (CCD) at zero applied strain is taken as the background signal, denoted $I_o$. An image of the LEDs taken under strain $\varepsilon$ is denoted $I_\varepsilon$. Fig. 15c shows enhancement factor $E$ of a single representative NW-LED ($E = (I_\varepsilon - I_o)/I_o$) as a function of applied strain up to $\varepsilon = -0.15\%$. $E$ is approximately linearly dependent on strain, and reaches 300% at a strain of $-0.15\%$, in agreement with theoretical results as long as the deformation of the ZnO nanowire is limited to the elastic range. The sensor sensitivity $S$ in terms of relative light intensity enhancement as a function of applied pressure could be defined as [71]

$$S = \frac{\Delta I/I}{\sigma} = \frac{\Delta I/I}{140(\text{GPa})|\varepsilon|} = \frac{E}{140|\varepsilon|} \quad \text{GPa}^{-1}$$

where $E$ is the enhancement factor, $\sigma$ the applied pressure, $\varepsilon$ the strain in ZnO NWs and 140 GPa is the Young's modulus for ZnO NWs. The sensitivity $S$ is hence found to be $\sim 12.88\ \text{GPa}^{-1}$.

The two-dimensional mapping of strain was demonstrated using a convex character pattern of 'PIEZO' molded on a sapphire substrate, which was directly applied onto the LED arrays as a seal (Fig. 16a). Fig. 16b presents an optical image of the device with an SU-8 convex mound on top. Each black dot is a pixel comprising a single ZnO NW-LED with 4 μm pitch. Light-emitting images of the device at applied strains of 0, $-0.06\%$ and $-0.15\%$ were recorded by a CCD, as shown in Fig. 16c–e, respectively. The images unambiguously show that the change in LED intensity occurred at the pixels that were being compressed by the molded pattern, while those not affected by the molded characters showed almost no change in LED intensity. There was little crosstalk between adjacent pixels in the device. The spatial strain distribution can be extracted from the LED intensity images. By carefully aligning the two images in Fig. 16c and e, an image for the enhancement factor $E(x, y) = [I_\varepsilon(x, y) - I_o(x, y)]/I_o(x, y)$ was obtained in Fig. 16f, where $(x,y)$ are the coordinates of the CCD pixels in the plane. The $E$ image provides a spatial mapping of pressure applied to the entire array, and clearly shows the word 'PIEZO', originating from the mold. The color code indicates that the average enhancement factor $E$ is ~200%. The signal-to-noise ratio of the $E$ factor can be derived using the line profile data, as indicated for two positions in Fig. 16e — one on the molded pattern (vertical pink line) and the other off the pattern (horizontal red line). The results are presented in Fig. 16g and h, respectively. The crosstalk is completely negligible. The $E$ factor for the seven NW-LED pixels on the mold increased by a factor of 4–5 (up to 750%) when the applied strain increased from $-0.06\%$ to $-0.15\%$ (Fig. 16g). In contrast, the 36 NW-LED pixels that were off the mold pattern showed no enhancement at all, instead having a random variation at the noise level when the strain was increased from $-0.06\%$ to $-0.15\%$ (Fig. 16h). This unambiguously shows the gigantic effect of the piezoelectricity on LED emission. It proves the principle of using the piezotronic effect for mapping pressure/strain at high spatial resolution, with high sensitivity and even high reliability.

The piezoelectric NW-LED-based approach offers a few unique advantages for imaging strain distribution. First, in contrast to other approaches such as cross-bar electrodes [71,72,74], where the pixels are the matrix defined by the electrodes so that the signal is measured and recorded in a sequential scanning mode, our pixels are defined by the distribution of NWs on the substrate, all of which share two common electrodes. In this way, mapping is carried out simultaneously for all pixels at a time resolution of ~90 ms. The above parallel detection technology offers a much faster mapping rate for creating pressure distribution maps, and the time resolution is almost dictated by the relaxation process in applying/retracting the strain. Furthermore, our fabrication procedure could be simpler and cheaper than for the cross-bar electrode arrangement. Second, the spatial resolution is much higher and can be improved by optimizing the size and distribution of nanowires. The diameter of our nanowires was ~1.5 μm, the estimated resolution for our devices is given by $R(\mu\text{m}) = D + 1.2(\mu\text{m})$, where $D$ (μm) is the diameter of the NWs. If the diameter were reduced to 100 nm, we could obtain a resolution of 1.3 μm. Third, although our current study is based on a hard substrate, it is possible to extend the current approach to a soft substrate by directly cutting the current device into smaller units and then transferring these onto a soft substrate to follow a certain pattern. Alternatively, we could fabricate ZnO $p$–$n$ homojunction arrays on any substrate (such as polydimethylsiloxane (PDMS) or fiber). Finally, although there are some variations in the lighting intensity in different nanowires before strain is applied, possibly due to fluctuations in junction quality, such 'background' information can be removed using a signal-processing technique, such as defining an enhancement factor with a relative change of NW intensity before and after straining. Furthermore, growing high-quality NWs using high-temperature vapor phase techniques, such as metal-organic chemical vapor deposition (MOCVD), may also help to improve mapping quality.

The above approach is scientifically new because it relies on the piezoelectric polarization charges for designing a stable, fast response, as well as parallel-detection strain-sensor arrays. The output signal is electroluminescence light, which is easy to integrate with photonic technologies for fast data transmission, processing and recording, and may enable the development of highly intelligent human-machine interfaces. This may represent a major step toward on-chip recording of mechanical signals by optical means, with potential applications in touchpad technology, personalized signatures, bio-imaging and optical MEMS. Furthermore, with the feasibility of fabricating ZnO nanowires on flexible substrates, the current approach could be extended to smart skin, which will have a great future in biological sciences, human–machine interfacing,

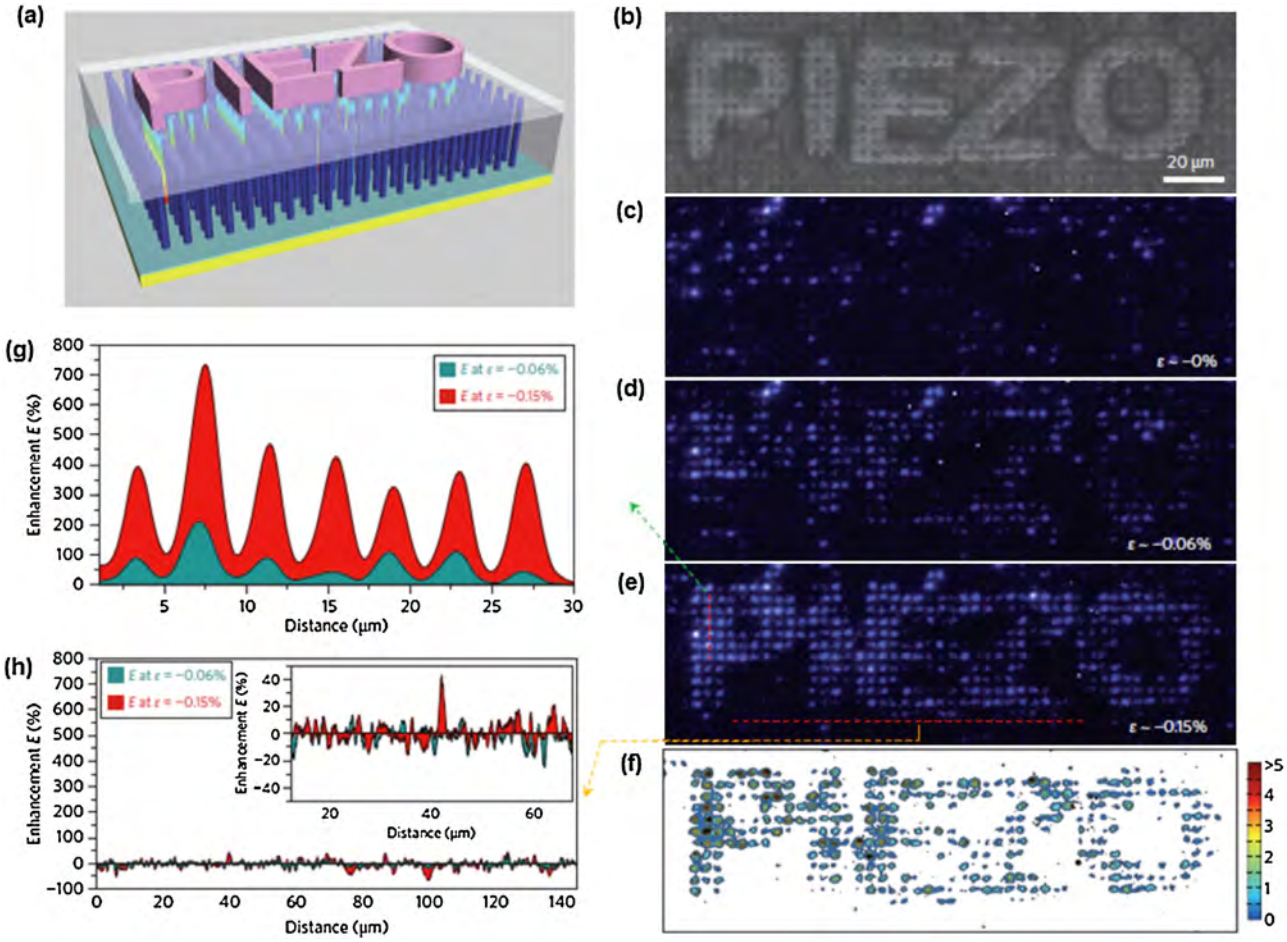


**Figure 16** (a) Illustration showing the working process of pressure distribution imaging. (b) Optical image of the device with a convex mold on top. (c—e) Electroluminescence images of the device at strains of 0, −0.06% and −0.15%, respectively. The images clearly show that a change in LED intensity occurred at the pixels that were compressed, while those away from the molded pattern showed almost no change. (f) Two-dimensional contour map of the $E(x,y)$ factor derived from the LED intensity images shown in (c) and (e). It directly presents the word 'PIEZO', as given on the mold. (g and h) Line profile data showing the signal-to noise ratio of the E factor for two typical positions-one on the molded pattern (vertical pink line, g) and one off the pattern (horizontal red line, (h) showing unambiguous differences. (For interpretation of the references to color in this figure legend, the reader is referred to the web version of the article.)
Reprinted with permission from [91]. Copyright 2013 Nature Publishing Group.

smart sensor and processor systems, and even defense technology.

## Application prospects

Piezoelectric semiconductors has been widely utilized in the GaN/AlGaN high electron mobility transistors (HEMTs) and similar effect of piezoelectric polarization on carrier properties, such as formation of two-dimensional electron gas (2DEG) with extremely high carrier concentration at the heterojunction interface, has been previously observed in HEMT device [94—96]. Theoretical investigation also reveals that appreciable piezoelectric field may be induced inside the nanowire heterostructures due to lattice mismatch, which can introduce significant effects on the charge carrier transport and confinement [86,97]. These piezoelectric fields, whereas, are fixed as introduced by interface strain and remain unchanged once the heterojunction devices are fabricated. In contrast, the mechanical flexibility of piezoelectric compound structures on soft substrates enables more versatile utilization of piezotronic effect in semiconductors for functional applications.

The essence of the emerging research and applications in piezotronics relies on the coupling between strain-induced polarization and semiconductor properties in piezoelectric semiconductor materials. Fundamental research of piezotronics as well as applications utilizing piezotronic effect introduce new concepts/understandings to classic semiconductor physics by taking into account the contributions from piezoelectric polarization to the charge carrier distribution and band structure adjustment (Fig. 17). In addition to the electronics and sensing applications shown here in this review, the presence of localized piezoelectric polarization charges can significantly modulate/control the charge carrier generation, separation, transport and/or recombination at an interface/junction

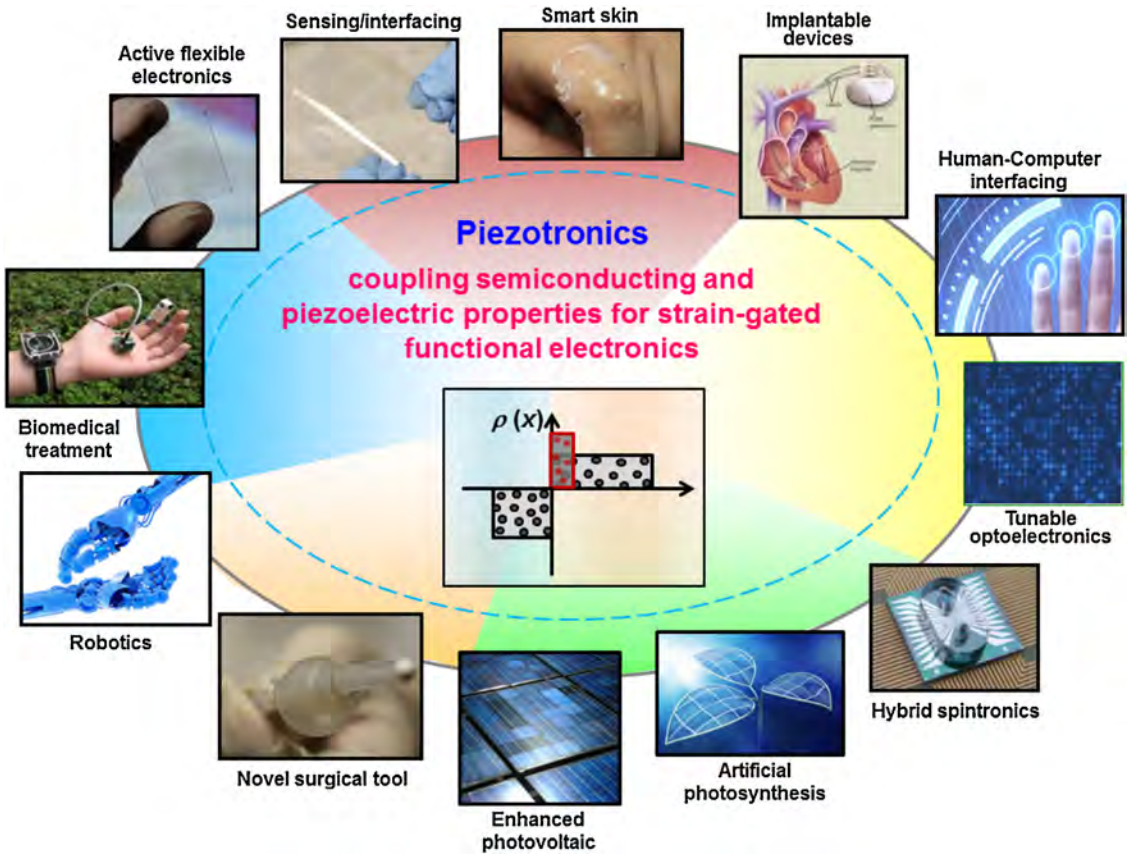


**Figure 17** Schematic diagram showing the prospects of utilizing piezotronic effect, which couples piezoelectric and semiconducting properties of piezoelectric semiconductor materials, for implementing many novel applications in tunable electronics, optoelectronics, spintronics, artificial photosynthesis and many other areas.

in optoelectronic processes [8,9,67,98,99]. The strain-induced electric fields have been demonstrated to be sufficiently large to impose a significant change in the confined energy states of strained-layer quantum wells [100—102], which may enable novel piezotronic devices based on heterogeneous nanostructures (e.g. core/shell or axial *p—n* junctions). Interfacial strain-induced polarization charges can also assist the catalytic process and modulate the electrochemical activity of related materials by adjusting the difference between the electrochemical potentials in the systems, which could give rise to piezo-enhanced catalysis or photosynthesis [103—106]. Controllable modulation of M-S contact or *p—n* junction by strain-induced polarization offers unprecedented method in addition to the conventional electrical controlling for implementing novel electronics, optoelectronics or even spin injection/transport in spintronics applications [107—110] which possess tunable operation characteristics adaptive to the ambient these devices are deployed. Piezotronics enables the novel approach for modulating device characteristics by tuning the junction/contact properties, which has been unavailable in conventional technologies without modifying the interface structure or chemistry. We have demonstrated here the advances from single piezotronic nanodevices to an array of devices and eventually to an integrated functional piezotronic system, which is a landmark progress in the field of nanotechnology. It is prospected that piezotronics will enable technology advances in sensing, human—electronics interfacing, robotics, biomedical diagnosis/therapy and prosthetics.

## Acknowledgements

The authors thank the support of NSF, DARPA, NIH and Chinese Academy of Sciences. We sincerely thank the following colleagues who made significant contributions to the work presented here: (not in particular order): Jun Zhou, Youfan Hu, Xudong Wang, Qing Yang, Ying Liu, Jr-Hau He, Yifan Gao, Weihua Han, Yusheng Zhou, Simiao Niu and many others.

## References

[1] H.C. Ko, M.P. Stoykovich, J.Z. Song, V. Malyarchuk, W.M. Choi, C.J. Yu, J.B. Geddes, J.L. Xiao, S.D. Wang, Y.G. Huang, J.A. Rogers, Nature 454 (2008) 748—753.
[2] B.Z. Tian, J. Liu, T. Dvir, L.H. Jin, J.H. Tsui, Q. Qing, Z.G. Suo, R. Langer, D.S. Kohane, C.M. Lieber, Nat. Mater. 11 (2012) 986—994.
[3] C. Wang, D. Hwang, Z. Yu, K. Takei, J. Park, T. Chen, B. Ma, A. Javey, Nat. Mater. 12 (2013) 899—904.
[4] C. Keplinger, J.-Y. Sun, C.C. Foo, P. Rothemund, G.M. Whitesides, Z. Suo, Science 341 (2013) 984—987.
[5] T. Dvir, B.P. Timko, M.D. Brigham, S.R. Naik, S.S. Karajanagi, O. Levy, H.W. Jin, K.K. Parker, R. Langer, D.S. Kohane, Nat. Nanotechnol. 6 (2011) 720—725.
[6] W.Z. Wu, X.N. Wen, Z.L. Wang, Science 340 (2013) 952—957.

[7] A.P. Alivisatos, A.M. Andrews, E.S. Boyden, M. Chun, G.M. Church, K. Deisseroth, J.P. Donoghue, S.E. Fraser, J. Lippincott-Schwartz, L.L. Looger, S. Masmanidis, P.L. McEuen, A.V. Nurmikko, H. Park, D.S. Peterka, C. Reid, M.L. Roukes, A. Scherer, M. Schnitzer, T.J. Sejnowski, K.L. Shepard, D. Tsao, G. Turrigiano, P.S. Weiss, C. Xu, R. Yuste, X.W. Zhuang, ACS Nano 7 (2013) 1850—1866.
[8] Z.L. Wang, Adv. Mater. 24 (2012) 4632—4646.
[9] Z.L. Wang, Piezotronics and Piezo-Phototronics, Springer, Berlin, Heidelberg, 2013.
[10] Z.L. Wang, W.Z. Wu, Angew. Chem. Int. Ed. 51 (2012) 11700—11721.
[11] G. Gautschi, Piezoelectric Sensorics: Force, Strain, Pressure, Acceleration and Acoustic Emission Sensors, Materials and Amplifiers, Springer, Berlin, Heidelberg, 2002.
[12] Z.L. Wang, Nano Today 5 (2010) 540—552.
[13] Z.L. Wang, Adv. Mater. 19 (2007) 889—892.
[14] X.D. Wang, J. Zhou, J.H. Song, J. Liu, N.S. Xu, Z.L. Wang, Nano Lett. 6 (2006) 2768—2772.
[15] Z.Y. Gao, J. Zhou, Y.D. Gu, P. Fei, Y. Hao, G. Bao, Z.L. Wang, J. Appl. Phys. 105 (2009) 113707.
[16] L. Schmidt-Mende, J.L. MacManus-Driscoll, Mater. Today 10 (2007) 40—48.
[17] Y. Gao, Z.L. Wang, Nano Lett. 9 (2009) 1103—1110.
[18] Z.L. Wang, J.H. Song, Science 312 (2006) 242—246.
[19] D.J. Bayerl, X.D. Wang, Adv. Funct. Mater. 22 (2012) 652—660.
[20] M.P. Lu, J. Song, M.Y. Lu, M.T. Chen, Y. Gao, L.J. Chen, Z.L. Wang, Nano Lett. 9 (2009) 1223—1227.
[21] G.D. Yuan, W.J. Zhang, J.S. Jie, X. Fan, J.A. Zapien, Y.H. Leung, L.B. Luo, P.F. Wang, C.S. Lee, S.T. Lee, Nano Lett. 8 (2008) 2591—2597.
[22] F. Wang, J.H. Seo, D. Bayerl, J.A. Shi, H.Y. Mi, Z.Q. Ma, D.Y. Zhao, Y.C. Shuai, W.D. Zhou, X.D. Wang, Nanotechnology 22 (2011) 225602.
[23] K.C. Pradel, W.Z. Wu, Y.S. Zhou, X.N. Wen, Y. Ding, Z.L. Wang, Nano Lett. 13 (2013) 2647—2653.
[24] A.B. Yankovich, B. Puchala, F. Wang, J.H. Seo, D. Morgan, X.D. Wang, Z.Q. Ma, A.V. Kvit, P.M. Voyles, Nano Lett. 12 (2012) 1311—1316.
[25] Z.L. Wang, MRS Bull. 37 (2012) 814—827.
[26] X.D. Wang, Am. Ceram. Soc. Bull. 92 (2013) 18—23.
[27] J. Shi, M.B. Starr, X.D. Wang, Adv. Mater. 24 (2012) 4683—4691.
[28] Y. Zhang, Y. Liu, Z.L. Wang, Adv. Mater. 23 (2011) 3004—3013.
[29] H.D. Espinosa, R.A. Bernal, M. Minary-Jolandan, Adv. Mater. 24 (2012) 4656—4675.
[30] R.T. Tung, Mater. Sci. Eng. R 35 (2001) 1—138.
[31] E.H. Rhoderick, R.H. Williams, Metal—Semiconductor Contacts, 2nd ed., Clarendon Press, Oxford, 1988.
[32] L.J. Brillson, Y.C. Lu, J. Appl. Phys. 109 (2011) 121301.
[33] Z.L. Wang, Adv. Mater. 24 (2012) 4630—4631.
[34] C.R. Crowell, S.M. Sze, Solid State Electron. 9 (1966) 1035.
[35] W.Z. Wu, Y.G. Wei, Z.L. Wang, Adv. Mater. 22 (2010) 4711.
[36] W.H. Han, Y.S. Zhou, Y. Zhang, C.Y. Chen, L. Lin, X. Wang, S.H. Wang, Z.L. Wang, ACS Nano 6 (2012) 3760—3766.
[37] R.S. Muller, T.I. Kamins, M. Chan, Device Electronics for Integrated Circuits, 3rd ed., John Wiley & Sons, Inc., New York, NY, 2003.
[38] J. Zhou, Y.D. Gu, P. Fei, W.J. Mai, Y.F. Gao, R.S. Yang, G. Bao, Z.L. Wang, Nano Lett. 8 (2008) 3035—3040.
[39] J. Zhou, P. Fei, Y.D. Gu, W.J. Mai, Y.F. Gao, R. Yang, G. Bao, Z.L. Wang, Nano Lett. 8 (2008) 3973—3977.
[40] P. Fei, P.H. Yeh, J. Zhou, S. Xu, Y.F. Gao, J.H. Song, Y.D. Gu, Y.Y. Huang, Z.L. Wang, Nano Lett. 9 (2009) 3435—3439.
[41] Y.S. Zhou, K. Wang, W.H. Han, S.C. Rai, Y. Zhang, Y. Ding, C.F. Pan, F. Zhang, W.L. Zhou, Z.L. Wang, ACS Nano 6 (2012) 6478—6482.
[42] W.H. Liu, M. Lee, L. Ding, J. Liu, Z.L. Wang, Nano Lett. 10 (2010) 3084—3089.
[43] R.M. Yu, W.Z. Wu, Y. Ding, Z.L. Wang, ACS Nano 7 (2013) 6403—6409.
[44] W.Z. Wu, Z.L. Wang, Nano Lett. 11 (2011) 2779—2785.
[45] J. Zhou, Y.D. Gu, Y.F. Hu, W.J. Mai, P.H. Yeh, G. Bao, A.K. Sood, D.L. Polla, Z.L. Wang, Appl. Phys. Lett. 94 (2009) 191103.
[46] P.H. Yeh, Z. Li, Z.L. Wang, Adv. Mater. 21 (2009) 4975—4978.
[47] T.Y. Wei, P.H. Yeh, S.Y. Lu, Z. Lin-Wang, J. Am. Chem. Soc. 131 (2009) 17690—17695.
[48] R. Yu, C. Pan, J. Chen, G. Zhu, Z.L. Wang, Adv. Funct. Mater. 23 (2013) 5868—5874.
[49] C.F. Pan, R.M. Yu, S.M. Niu, G. Zhu, Z.L. Wang, ACS Nano 7 (2013) 1803—1810.
[50] R.M. Yu, C.F. Pan, Z.L. Wang, Energ. Environ. Sci. 6 (2013) 494—499.
[51] S. Niu, Y. Hu, X. Wen, Y. Zhou, F. Zhang, L. Lin, S. Wang, Z.L. Wang, Adv. Mater. 25 (2013) 3701—3706.
[52] Y.G. Wei, W.Z. Wu, R. Guo, D.J. Yuan, S.M. Das, Z.L. Wang, Nano Lett. 10 (2010) 3414—3419.
[53] Y. Huang, X.F. Duan, Q.Q. Wei, C.M. Lieber, Science 291 (2001) 630—633.
[54] J. Wallentin, N. Anttu, D. Asoli, M. Huffman, I. Aberg, M.H. Magnusson, G. Siefer, P. Fuss-Kailuweit, F. Dimroth, B. Witzigmann, H.Q. Xu, L. Samuelson, K. Deppert, M.T. Borgstrom, Science 339 (2013) 1057—1060.
[55] D.J. Yuan, R. Guo, Y.G. Wei, W.Z. Wu, Y. Ding, Z.L. Wang, S.M. Das, Adv. Funct. Mater. 20 (2010) 3484—3489.
[56] X.N. Wen, W.Z. Wu, Y. Ding, Z.L. Wang, J. Mater. Chem. 22 (2012) 9469—9476.
[57] Y.S. Zhou, R. Hinchet, Y. Yang, G. Ardila, R. Songmuang, F. Zhang, Y. Zhang, W.H. Han, K. Pradel, L. Montes, M. Mouis, Z.L. Wang, Adv. Mater. 25 (2013) 883—888.
[58] R.M. Yu, L. Dong, C.F. Pan, S.M. Niu, H.F. Liu, W. Liu, S. Chua, D.Z. Chi, Z.L. Wang, Adv. Mater. 24 (2012) 3532—3537.
[59] J.M. Wu, C.Y. Chen, Y. Zhang, K.H. Chen, Y. Yang, Y.F. Hu, J.H. He, Z.L. Wang, ACS Nano 6 (2012) 4369—4374.
[60] L. Dong, S.M. Niu, C.F. Pan, R.M. Yu, Y. Zhang, Z.L. Wang, Adv. Mater. 24 (2012) 5470—5475.
[61] Y.F. Hu, Y. Zhang, L. Lin, Y. Ding, G. Zhu, Z.L. Wang, Nano Lett. 12 (2012) 3851—3856.
[62] X.N. Wen, W.Z. Wu, Y. Ding, Z.L. Wang, Adv. Mater. 25 (2013) 3371—3379.
[63] X.N. Wen, W.Z. Wu, Z.L. Wang, Nano Energy 2 (2013) 1093—1100.
[64] Q. Yang, Y. Liu, C.F. Pan, J. Chen, X.N. Wen, Z.L. Wang, Nano Lett. 13 (2013) 607—613.
[65] F. Zhang, Y. Ding, Y. Zhang, X.L. Zhang, Z.L. Wang, ACS Nano 6 (2012) 9229—9236.
[66] C.F. Pan, S.M. Niu, Y. Ding, L. Dong, R.M. Yu, Y. Liu, G. Zhu, Z.L. Wang, Nano Lett. 12 (2012) 3302—3307.
[67] Q. Yang, W.H. Wang, S. Xu, Z.L. Wang, Nano Lett. 11 (2011) 4012—4017.
[68] Q. Yang, X. Guo, W.H. Wang, Y. Zhang, S. Xu, D.H. Lien, Z.L. Wang, ACS Nano 4 (2010) 6285—6291.
[69] Y.F. Hu, Y. Zhang, Y.L. Chang, R.L. Snyder, Z.L. Wang, ACS Nano 4 (2010) 4220—4224.
[70] K. Ziegler-Graham, E.J. MacKenzie, P.L. Ephraim, T.G. Travison, R. Brookmeyer, Arch. Phys. Med. Rehabil. 89 (2008) 422—429.
[71] K. Takei, T. Takahashi, J.C. Ho, H. Ko, A.G. Gillies, P.W. Leu, R.S. Fearing, A. Javey, Nat. Mater. 9 (2010) 821—826.

[72] S.C.B. Mannsfeld, B.C.K. Tee, R.M. Stoltenberg, C.V.H.H. Chen, S. Barman, B.V.O. Muir, A.N. Sokolov, C. Reese, Z.N. Bao, Nat. Mater. 9 (2010) 859—864.
[73] T. Someya, T. Sekitani, S. Iba, Y. Kato, H. Kawaguchi, T. Sakurai, Proc. Natl. Acad. Sci. U.S.A. 101 (2004) 9966—9970.
[74] D.J. Lipomi, M. Vosgueritchian, B.C.K. Tee, S.L. Hellstrom, J.A. Lee, C.H. Fox, Z.N. Bao, Nat. Nanotechnol. 6 (2011) 788—792.
[75] D.H. Kim, N.S. Lu, R. Ma, Y.S. Kim, R.H. Kim, S.D. Wang, J. Wu, S.M. Won, H. Tao, A. Islam, K.J. Yu, T.I. Kim, R. Chowdhury, M. Ying, L.Z. Xu, M. Li, H.J. Chung, H. Keum, M. McCormick, P. Liu, Y.W. Zhang, F.G. Omenetto, Y.G. Huang, T. Coleman, J.A. Rogers, Science 333 (2011) 838—843.
[76] A. Javey, S. Nam, R.S. Friedman, H. Yan, C.M. Lieber, Nano Lett. 7 (2007) 773—777.
[77] J.H. Ahn, H.S. Kim, K.J. Lee, S. Jeon, S.J. Kang, Y.G. Sun, R.G. Nuzzo, J.A. Rogers, Science 314 (2006) 1754—1757.
[78] S. Nam, X.C. Jiang, Q.H. Xiong, D. Ham, C.M. Lieber, Proc. Natl. Acad. Sci. U.S.A. 106 (2009) 21035—21038.
[79] T. Bryllert, L.E. Wernersson, L.E. Froberg, L. Samuelson, IEEE Electron. Device Lett. 27 (2006) 323—325.
[80] T. Sekitani, T. Yokota, U. Zschieschang, H. Klauk, S. Bauer, K. Takeuchi, M. Takamiya, T. Sakurai, T. Someya, Science 326 (2009) 1516—1519.
[81] R.S. Johansson, A.B. Vallbo, J. Physiol. (Lond.) 286 (1979) 283—300.
[82] B. Nemeth, M.D. Symes, A.G. Boulay, C. Busche, G.J.T. Cooper, D.R.S. Cumming, L. Cronin, Adv. Mater. 24 (2012) 1238—1242.
[83] S.A. Mascaro, H.H. Asada, IEEE Trans. Robot. Autom. 17 (2001) 698—708.
[84] Y. Yang, W.X. Guo, Y. Zhang, Y. Ding, X. Wang, Z.L. Wang, Nano Lett. 11 (2011) 4812—4817.
[85] J. Shi, P. Zhao, X.D. Wang, Adv. Mater. 25 (2013) 916—921.
[86] F. Boxberg, N. Sondergaard, H.Q. Xu, Nano Lett. 10 (2010) 1108—1112.
[87] S.Z. Yang, L.F. Wang, X.Z. Tian, Z. Xu, W.L. Wang, X.D. Bai, E.G. Wang, Adv. Mater. 24 (2012) 4676—4682.
[88] P. Gao, Z.Z. Wang, K.H. Liu, Z. Xu, W.L. Wang, X.D. Bai, E.G. Wang, J. Mater. Chem. 19 (2009) 1002—1005.
[89] X.B. Han, L.Z. Kou, Z.H. Zhang, Z.Y. Zhang, X.L. Zhu, J. Xu, Z.M. Liao, W.L. Guo, D.P. Yu, Adv. Mater. 24 (2012) 4707—4711.
[90] S.G. Xu, W.H. Guo, S.W. Du, M.M.T. Loy, N. Wang, Nano Lett. 12 (2012) 5802—5807.
[91] C.F. Pan, L. Dong, G. Zhu, S.M. Niu, R.M. Yu, Q. Yang, Y. Liu, Z.L. Wang, Nat. Photon. 7 (2013) 752—758.
[92] D.K. Hwang, S.H. Kang, J.H. Lim, E.J. Yang, J.Y. Oh, J.H. Yang, S.J. Park, Appl. Phys. Lett. 86 (2005) 222101.
[93] Y. Zhang, Z.L. Wang, Adv. Mater. 24 (2012) 4712—4718.
[94] L. Hsu, W. Walukiewicz, J. Appl. Phys. 89 (2001) 1783—1789.
[95] E.T. Yu, X.Z. Dang, P.M. Asbeck, S.S. Lau, G.J. Sullivan, J. Vac. Sci. Technol. B 17 (1999) 1742—1749.
[96] O. Ambacher, J. Smart, J.R. Shealy, N.G. Weimann, K. Chu, M. Murphy, W.J. Schaff, L.F. Eastman, R. Dimitrov, L. Wittmer, M. Stutzmann, W. Rieger, J. Hilsenbeck, J. Appl. Phys. 85 (1999) 3222—3233.
[97] F. Boxberg, N. Sondergaard, H.Q. Xu, Adv. Mater. 24 (2012) 4692—4706.
[98] Y. Zhang, Y. Yang, Z.L. Wang, Energ. Environ. Sci. 5 (2012) 6850—6856.
[99] Y. Liu, Q. Yang, Y. Zhang, Z.Y. Yang, Z.L. Wang, Adv. Mater. 24 (2012) 1410—1417.
[100] C. Mailhiot, D.L. Smith, Phys. Rev. B 37 (1988) 10415—10418.
[101] D.L. Smith, C. Mailhiot, Phys. Rev. Lett. 58 (1987) 1264—1267.
[102] V.C. Stergiou, N.T. Pelekanos, Y.S. Raptis, Phys. Rev. B 67 (2003) 165304.
[103] M.B. Starr, J. Shi, X.D. Wang, Angew. Chem. Int. Ed. 51 (2012) 5962—5966.
[104] X.B. Chen, S.H. Shen, L.J. Guo, S.S. Mao, Chem. Rev. 110 (2010) 6503—6570.
[105] D. Gust, T.A. Moore, A.L. Moore, Acc. Chem. Res. 34 (2001) 40—48.
[106] A.J. Bard, M.A. Fox, Acc. Chem. Res. 28 (1995) 141—145.
[107] J.R. Chen, P.M. Odenthal, A.G. Swartz, G.C. Floyd, H. Wen, K.Y. Luo, R.K. Kawakami, Nano Lett. 13 (2013) 3106—3110.
[108] V. Garcia, M. Bibes, L. Bocher, S. Valencia, F. Kronast, A. Crassous, X. Moya, S. Enouz-Vedrenne, A. Gloter, D. Imhoff, C. Deranlot, N.D. Mathur, S. Fusil, K. Bouzehouane, A. Barthelemy, Science 327 (2010) 1106—1110.
[109] S.A. Wolf, D.D. Awschalom, R.A. Buhrman, J.M. Daughton, S. von Molnar, M.L. Roukes, A.Y. Chtchelkanova, D.M. Treger, Science 294 (2001) 1488—1495.
[110] I. Zutic, J. Fabian, S. Das Sarma, Rev. Mod. Phys. 76 (2004) 323—410.

**Dr. Wenzhuo Wu** is the postdoctoral fellow in School of Materials Science and Engineering at Georgia Institute of Technology. He received his B.S. in Electronic Information Science and Technology in 2005 from the University of Science and Technology of China (USTC), Hefei and his M.E. in Electrical and Computer Engineering from the National University of Singapore (NUS) in 2008. After working at Chartered Semiconductor Manufacturing (now GlobalFoundries) in Singapore from 2007 to 2008, he began the doctoral research under the supervision of Prof. Zhong Lin Wang and received his Ph.D. from Georgia Institute of Technology in Materials Science and Engineering in 2013. Wenzhuo's research interests include synthesis, fabrication and integration of nanomaterials/devices; nanotechnology-enabled applications in energy harvesting/conversion/storage, electronics, optoelectronics, sensing and interfacing; piezotronics/piezo-phototronics; self-powered micro/nano-systems.

**Caofeng Pan** received his B.S. degree (2005) and his Ph.D. (2010) in Materials Science and Engineering from Tsinghua University, China. He then joined in the group of Professor Zhong Lin Wang at the Georgia Institute of Technology as a postdoctal fellow. He is currently a professor and a group leader at Beijing Institute of Nanoenergy and Nanosystems, Chinese Academy of Sciences since 2013. His main research interests focus on the fields of piezotronics/piezo-phototronics for fabricating new electronic and optoelectronic devices, nano-power source (such as nanofuel cell, nano biofuel cell and nanogenerator), hybrid nanogenerators, and self-powered nanosystems. Details can be found at http://124.16.153.201:8000/index%20en.php.

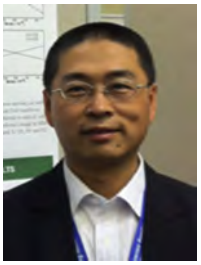

**Yan Zhang** received his degree (1995) and Ph.D degree in Theoretical Physics (2004) from Lanzhou University. Then, he worked as a lecturer and associate Professor (2007) of Institute of Theoretical Physics in Lanzhou University. In 2009 he worked as research scientist in the group of Professor Zhong Lin Wang at Georgia Institute of Technology. His main research interest and activities are: self-powered nano/micro system, theoretical calculation of piezotronic, dynamics of time-delay systems and complex networks.

**Xiaonan Wen** received his B.S. degree in Physics from Peking University, China in 2010. He is currently a Ph.D. student in the School of Materials Science & Engineering, Georgia Institute of Technology. His research interests include synthesis of functional nanomaterials, energy harvesting using piezoelectric and triboelectric generators, self-powered nanosystems, piezo-electronics and piezo-optoelectronics based on ZnO, GaN etc. for novel transistors, devices and integration of them into functional systems.

**Dr. Zhong Lin Wang** received his PhD from Arizona State University in 1987. He now is the Hightower Chair in Materials Science and Engineering and Regents' Professor at Georgia Tech. Dr. Wang has made original and innovative contributions to the synthesis, discovery, characterization and understanding of fundamental physical properties of oxide nanobelts and nanowires, as well as applications of nanowires in energy sciences, electronics, optoelectronics and biological science. His discovery and breakthroughs in developing nanogenerators establish the principle and technological road map for harvesting mechanical energy from environment and biological systems for powering a personal electronics. His research on self-powered nanosystems has inspired the worldwide effort in academia and industry for studying energy for micro—nano-systems, which is now a distinct disciplinary in energy research and future sensor networks. He coined and pioneered the field of piezotronics and piezo-phototronics by introducing piezoelectric potential gated charge transport process in fabricating new electronic and optoelectronic devices. This breakthrough by redesign CMOS transistor has important applications in smart MEMS/NEMS, nanorobotics, human-electronics interface and sensors. Dr. Wang's publications have been cited for over 62,000 times. The H-index of his citations is 122. Dr. Wang was elected as a foreign member of the Chinese Academy of Sciences in 2009, member of European Academy of Sciences in 2002, fellow of American Physical Society in 2005, fellow of AAAS in 2006, fellow of Materials Research Society in 2008, fellow of Microscopy Society of America in 2010, and fellow of the World Innovation Foundation in 2002. He received 2014 the James C. McGroddy Prize for New Materials from America Physical Society, 2013 ACS Nano Lectureship award, 2012 Edward Orton Memorial Lecture Award and 2009 Purdy Award from American Ceramic Society, 2011 MRS Medal from the Materials Research Society, 1999 Burton Medal from Microscopy Society of America. Details can be found at: http://www.nanoscience.gatech.edu.